Journal of Energy Storage 83 (2024) 110683

Contents lists available at ScienceDirect

Journal of Energy Storage

journal homepage: www.elsevier.com/locate/est

Research papers

Aerosol-assisted synthesis of 3D hybridized reduced graphene oxide-carbon nanotube composite microsphere with cobalt-iron selenide nanocrystal as anode materials for potassium-ion batteries

Sang-Hyun Kim [a,1], Tae Ha Kim [a,1], Hyeon Ki Park [b], Yun Chan Kang [c], Jung Sang Cho [d], Gi Dae Park [a,*]

[a] Department of Advanced Material Engineering, Chungbuk National University, Chungbuk 361-763, Republic of Korea
[b] Research and Development Team, SOLE Materials Co., Ltd, 62, Hugi-gil, Ochang-eup, Cheongwon-gu, Cheongju-si, Chungbuk 28105, Republic of Korea
[c] Department of Materials Science and Engineering, Korea University, Anam-Dong, Seongbuk-Gu, Seoul 136-713, Republic of Korea
[d] Department of Engineering Chemistry, Chungbuk National University, Chungbuk 361-763, Republic of Korea

ARTICLE INFO

Keywords:
Potassium ion batteries
Transition metal selenide
Graphene
Carbon nanotube
Electrolytes

ABSTRACT

The combined strategies involving graphene and carbon nanotubes (CNTs) have garnered significant attention as a clever approach to address the inherent tendency of graphene to irreversibly aggregate due to strong van der Waals interactions. Recently, a notable method for crafting graphene-CNT composites has emerged, wherein CNTs are grown perpendicular to the graphene surface using catalysts like transition metal nanocrystals via chemical vapor deposition (CVD) techniques. In this study, we propose a novel anode material for potassium-ion batteries: a three-dimensionally hybridized composite microsphere comprising cobalt-iron selenide, reduced graphene oxide (rGO), and carbon nanotubes (CNTs). This novel material was introduced for the first time, employing both spray pyrolysis and CVD processes. The spray pyrolysis step was employed to generate crumpled rGO microspheres, effectively mitigating graphene's tendency to stack. The CNTs grown atop the rGO surface further acted as a barrier to prevent stacking. The bimetallic cobalt-iron nanocrystals enveloped in graphitic carbon were subsequently transformed into cobalt-iron selenide through a straightforward selenization process, enhancing its potential for potassium-ion storage. The resulting cobalt-iron selenide-rGO-CNT composite anode exhibited exceptional capacity and remarkable stability in cycling performance, outperforming the cobalt-iron selenide-rGO composite. To optimize the properties of these developed electrode materials, additional evaluations were undertaken to assess their characteristics based on the specific electrolyte type employed in potassium-ion batteries.

1. Introduction

Graphene, as a two-dimensional material, has attracted significant research interest due to its unique structural, mechanical, and optical properties, as well as its high thermal conductivity and outstanding electrical properties [1–5]. However, a major challenge for its applications, particularly in energy-related fields, is the tendency of graphene to form irreversible restacked aggregates due to strong van der Waals interaction [6–8]. To address this issue, several strategies have been introduced to minimize graphene restacking, primarily by inserting a

Abbreviations: CNT, carbon nanotube; CVD, chemical vapor deposition; rGO, reduced graphene oxide; GO, graphene oxide; PS, polystyrene; DCDA, dicyandiamide; SEM, scanning electron microscopy; XRD, X–ray diffraction; TEM, transmission electron microscopy; SAED, selected area electron diffraction; XPS, X–ray photoelectron spectroscopy; BET, Brunauer–Emmett–Teller; BJH, Barrett–Joyner–Halenda; TG, thermogravimetric; DME, 1,2–dimethoxyethane; EC, ethyl carbonate; KFSI, potassium bis(fluorosulfonyl)imide; DEC, diethyl carbonate; CV, cyclic voltammetry; SEI, solid electrolyte interphase; ICE, initial Coulombic efficiency; EIS, electrochemical impedance spectroscopy; R_s, solution resistance; R_{sei}, SEI layer resistance; R_{ct}, charge transfer resistance; CPE_{sei}, constant phase element of SEI capacitance; CPE_{dl}, constant phase element of electric double layer; R_{tot}, total resistance; CE, Coulombic efficiency; GITT, galvanostatic intermittent titration technique; D_{K+}, potassium-ion diffusion coefficient.

* Corresponding author.
E-mail address: gdpark@chungbuk.ac.kr (G.D. Park).
[1] These authors contributed equally to this work.

https://doi.org/10.1016/j.est.2024.110683
Received 17 October 2023; Received in revised form 4 January 2024; Accepted 28 January 2024
Available online 3 February 2024

spacer between graphene layers [9–12]. The spacer not only helps to mitigate agglomeration but also contributes to the overall surface area and conductivity of the active material, thereby enhancing its functionality. A recent approach to achieve this is through the composite strategy of graphene and carbon nanotubes (CNTs), which serves as a new method for introducing a spacer [13–15]. This composite strategy enables the combination of the unique properties of both graphene and CNTs.

Various methods have been reported for hybridization of carbon nanotubes (CNTs) and graphene. One representative strategy involves the physical uniform mixing of graphene nanosheets and CNTs. Several techniques, such as layer-by-layer assembly, vacuum filtration, electrophoretic deposition, microwave synthesis, freeze-drying, hydrothermal, and solvothermal routes, have been introduced to prepare graphene-CNT composites using a mixed graphene/CNT solution [16–22]. To achieve a uniform graphene-CNT composite, it is crucial to optimize the size of the graphene nanosheets, as well as the length, diameter, and highly dispersed state of the CNTs in the colloidal solution. However, the physical mixing method of graphene and CNTs has limitations in completely preventing graphene restacking and faces difficulties in obtaining a homogeneous composite.

Recently, a method that has garnered attention for synthesizing graphene-CNT composites involves the growth of CNTs perpendicular to the graphene surface using catalysts such as transition metal nanocrystals through chemical vapor deposition (CVD) methods. In this composite, graphene and CNTs are interconnected by catalyst nanoparticles [23], which reduce interfacial electrical and thermal resistances, resulting in favorable out-of-plane mechanical and electrical properties while preserving the excellent in-plane properties of graphene without stacking. Various graphene composites grown with CNTs have been reported as anode materials for alkali-ion batteries, demonstrating improved properties [24,25]. Furthermore, research findings have indicated capacity enhancement through the incorporation of metal compound nanocrystals in addition to the alkali-ion storage offered by the graphene-CNT composite itself [26].

In this study, a novel three-dimensionally hybridized cobalt-iron selenide-reduced graphene oxide (rGO)-carbon nanotube (CNT) composite microsphere was suggested for the first time, prepared by applying spray pyrolysis and CVD processes. The spray pyrolysis process was employed to produce crumpled rGO microspheres, which effectively mitigated the graphene stacking issue reported in previous literatures [27–29]. Using cobalt and iron metal nanocrystal catalysts, CNTs were uniformly grown on the surface of the crumpled rGO, leading to the formation of cobalt-iron selenide-rGO-CNT microspheres through a subsequent selenization process. In this research, the application of an anode material for potassium-ion batteries of metal selenide and rGO-CNT composite with a three-dimensional spherical shape was firstly studied. To demonstrate the superiority of the material, a cobalt-iron selenide-rGO composite without CNT growth was prepared as a comparative sample. To optimize the properties of the developed electrode materials, an evaluation was additionally conducted to assess their characteristics based on the specific electrolyte type used in potassium-ion batteries.

2. Experimental

2.1. Materials synthesis

Three-dimensional crumpled graphene ball was prepared via spray pyrolysis. The spray solution was prepared by dissolving a 1:1 ratio of 0.04 M cobalt nitrate hexahydrate and iron nitrate nonahydrate, along with 1 mg mL^{-1} of the graphene oxide (GO) and 1 g of mL^{-1} of 100 nm sized polystyrene (PS) nanobeads in 500 mL of distilled water. GO was synthesized using a modified Hummer's method [30], and simultaneously, PS nanobead was generated through an emulsion polymerization technique [31], which was utilized as pore generator. During the spray pyrolysis, droplets were generated using a 1.7-MHz ultrasonic spray generator, consisting of six vibrators. These droplets were then transported into a quartz reactor, which had a length of 1200 mm and diameter of 50 mm. The reactor was maintained at 400 °C, and air was used as the carrier gas at a flow rate of 20 L min^{-1}. The resulting spray precursor and dicyandiamide (DCDA) were subjected to a CVD process in tube furnace. The first step involved heating at 300 °C 3 h, followed by 750 °C 2 h at a rate of 5 °C min^{-1} under 10 % H_2/Ar atmosphere. This process led to the synthesis of CoFe-rGO-CNT. Subsequently, a post treatment involving selenium powder at 400 °C 12 h at a rate of 5 °C min^{-1} under 10 % H_2/Ar atmosphere, resulting in the formation of (CoFe)Se_x-rGO-CNT. Furthermore, an alternative synthesis route was employed to produce (CoFe)Se_x-rGO, where the sprayed precursor underwent selenization at the same condition as previously mentioned, but without the intermediate CVD process. Detailed information pertaining to the characterization and electrochemical measurements of the prepared samples is provided in Supporting information.

3. Results and discussion

3.1. Physical characterization results

The formation mechanism of three-dimensionally hybridized cobalt-iron selenide-reduced graphene oxide (rGO)-carbon nanotube (CNT) composite microsphere was exhibited in Scheme 1. The spray pyrolysis process facilitated the formation of crumpled reduced graphene oxide microsphere using a spray solution containing dissolved cobalt, iron nitrate, polystyrene (PS) nanobeads and highly dispersed graphene oxide nanosheets. During the spray pyrolysis, graphene oxide (GO) nanosheets were transformed into crumpled reduced graphene oxide microspheres, simultaneously cobalt-iron oxide nanocrystals were distributed on the rGO surface and composited with PS nanobeads. The composite of PS nanobeads helped to improve the sphericity of graphene balls. The prepared cobalt-iron oxide-rGO-PS nanobeads composite microsphere was post-treated with dicyandiamide (DCDA), which decomposed into carbon nitride gas in a reducing atmosphere. During this process, cobalt-iron oxide nanocrystals decorated on the rGO matrix were reduced to cobalt-iron alloy nanocrystals and simultaneously dispersed PS nanobeads were decomposed to form porous structure inside microsphere. The formation of metallic cobalt-iron nanocrystals facilitated nitrogen-doped CNT growth through the catalyst effect, as well as the formation of a graphitic carbon ring surrounding the cobalt-iron alloy nanocrystals [32]. Concurrently, the porous voids, which were derived from decomposition of PS nanobeads, provided space for CNTs to grow sufficiently inside the microsphere. Finally, three-dimensionally hybridized cobalt-iron selenide-reduced graphene oxide (rGO)-carbon nanotube (CNT) composite microsphere was obtained through a simple selenization process. For the comparative sample, the sprayed precursor was directly selenized to form cobalt-iron selenide-rGO composite microsphere.

The morphological characteristic of the sprayed precursor powders was shown in Fig. S1. The typical 2d structured graphene sheets were transformed into an overall crumpled graphene ball structure , as confirmed by the low-magnified SEM image in Fig. S1a and their mean size was 0.91 μm. In the high-magnification SEM image in Fig. S1b, few crystals were discernible on the rGO microsphere surface, which might be because cobalt-iron oxide nanocrystals were a very small size on the order of nanodots. It could be explained by the broad XRD pattern of the sprayed precursor in Fig. S1c. In addition, it could be verified that the composite of PS nanobeads improved the sphericity of rGO microspheres. The sprayed precursor was transformed into cobalt-iron alloy-rGO-CNT microsphere (denoted as CoFe-rGO-CNT) through post-treatment using DCDA and its morphological and crystal structural characteristics were exhibited in Figs. 1 and S2. The low-magnified SEM image in Fig. 1a clearly showed short CNTs uniformly grown on the surface of the microsphere compared to the smooth-surfaced sprayed

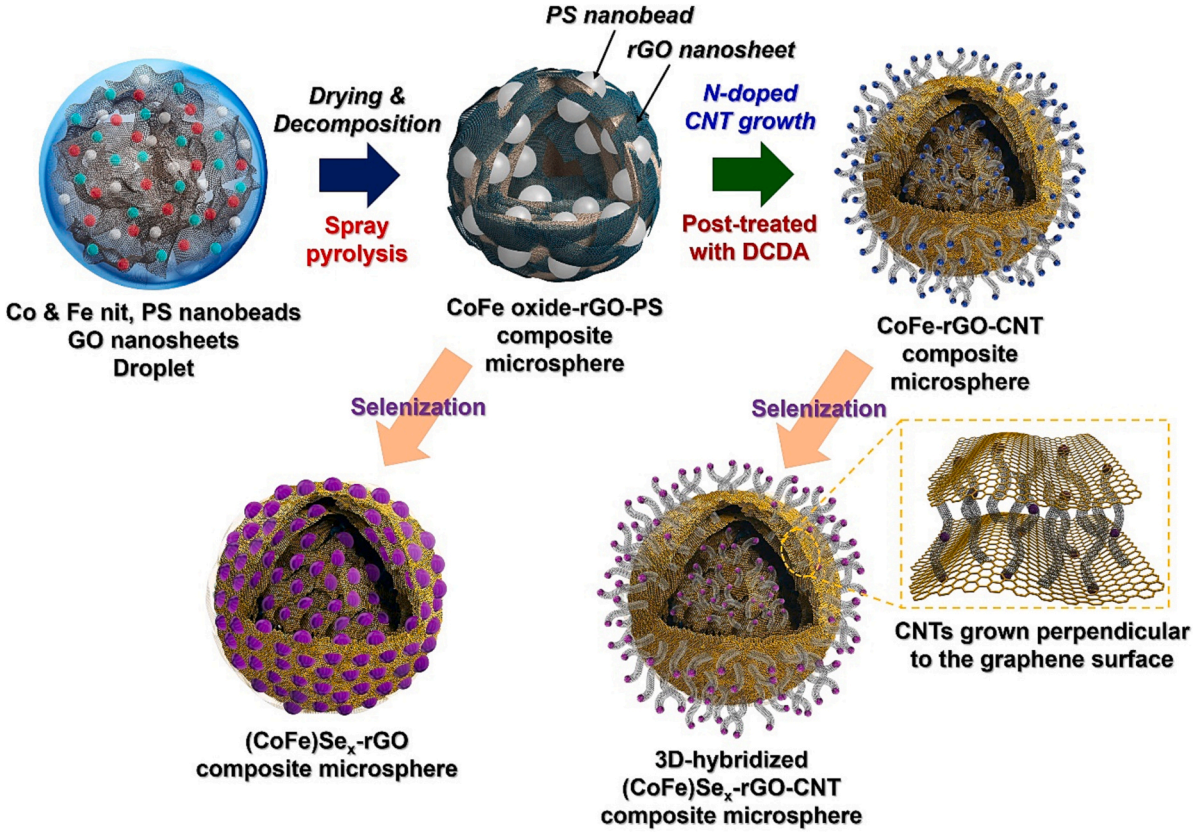

Scheme 1. The schematic illustration of the synthesis process for (CoFe)Se$_x$-rGO-CNT microsphere and (CoFe)Se$_x$-rGO microsphere.

precursor rGO microsphere in Fig. S1. It confirmed the production of a hierarchically porous structured microsphere through the growth of the CNTs on the surface of crumpled rGO matrix. TEM images in Fig. 1b and c revealed that CNTs were uniformly grown on the surface of the inner rGO, which constituted the crumpled rGO microsphere. It could be expected that the nanocrystals uniformly distributed throughout the microsphere are cobalt-iron alloy, which acts as a catalyst for growing CNTs [33]. Some core-shell structured nanocrystals are formed through the Kirkendall effect, resulting from the partial oxidation of the cobalt-iron alloy during the TEM sample preparation process [29]. Additionally, crystals of cobalt-iron alloy are variously observed at the starting point, mid-point, and end-point of CNTs, as indicated by the arrows in Fig. 1c. The high-resolution TEM image in Fig. 1d revealed clear lattice fringes separated by 0.21 and 0.20 nm corresponding to the (330) and (110) crystal planes of $Co_{0.72}Fe_{0.28}$, and Co_3Fe_7 alloys phases, respectively. The selected area electron diffraction (SAED) and XRD pattern in Figs. 1e and S2, respectively, revealed the formation of $Co_{0.72}Fe_{0.28}$, and Co_3Fe_7 alloys phases. The elemental mapping images in Fig. 1f showed cobalt-iron alloys decorated on carbon matrix.

The morphologies of the three-dimensionally hybridized cobalt-iron selenide-reduced graphene oxide (rGO)-carbon nanotube (CNT) composite microsphere (denoted as (CoFe)Se$_x$-rGO-CNT), which were prepared by selenization from cobalt-iron alloy-rGO-CNT microsphere, are represented in Fig. 2. The low-magnified SEM image in Fig. 2a showed that the microspheres remained hierarchically porous overall compared to the CoFe-rGO-CNT in Fig. 1a. The TEM images in Fig. 2b and c revealed that small-sized cobalt-iron alloys were transformed into slightly more crystalline grown cobalt-iron selenide, and their nanocrystals were uniformly distributed over the rGO-CNT composite microsphere. The mean size of the cobalt-iron selenide nanocrystals was calculated to be 59.1 nm. Moreover, a developed hierarchical structure of CNTs connected the microspheres. The high-resolution TEM image in Fig. 2d exhibited clear lattice fringes separated by 0.19 and 0.25 nm of a (CoFe)Se_2 solid solution, which correspond well to the (121) and (111) crystal planes of $CoSe_2$ and $FeSe_2$ phases, respectively [34]. The SAED pattern in Fig. 2e additionally confirmed the formation of (CoFe)Se_2 solid solution. The elemental mapping image in Fig. 2f showed that the cobalt-iron selenide nanocrystals were distributed over the carbon matrix of rGO and CNTs. The N signal was related to nitrogen-doped CNT, derived from decomposition of DCDA. N-doped CNT could contribute to enhancing the electrical conductivity of electrode materials [35,36].

The morphological properties of the cobalt-iron selenide-rGO composite microsphere (denoted as (CoFe)Se$_x$-rGO) as comparative sample were displayed in Fig. 3. The low-magnified SEM image at Fig. 3a exhibited nanocrystals grown on the surface with a shape similar to that of the sprayed precursor in Fig. S1. The TEM images in Fig. 3b and c showed the uniform distribution of cobalt-iron selenide nanocrystals on the crumpled rGO microsphere. The mean size of cobalt-iron selenide nanocrystals was calculated as 98.2 nm, which was larger than that of (CoFe)Se$_x$-rGO-CNT. It was revealed that the graphitic carbon formed around CoFe alloy nanocrystal suppressed the crystal growth in the process of crystallization into cobalt-iron selenide. The high-resolution TEM image in Fig. 3d exhibited clear lattice fringes separated by 0.19 and 0.25 nm of a (CoFe)Se_2 solid solution, which correspond well to the (121) and (111) crystal planes of $CoSe_2$ and $FeSe_2$ phases, respectively. The SAED pattern in Fig. 3e additionally confirmed the formation of (CoFe)Se_2 solid solution. The elemental mapping images in Fig. 3f showed that cobalt-iron selenide nanocrystals were distributed over the rGO.

The crystal structures of (CoFe)Se$_x$-rGO-CNT and (CoFe)Se$_x$-rGO were analyzed by XRD as shown in Fig. 4a. Both samples match well with the $FeSe_2$ phase, but the down shifting of XRD peaks was observed. This is due to the enhancements in lattice parameters caused by that Co^{2+} has a larger ionic radius than Fe^{2+} [37,38]. However, in the XRD pattern of (CoFe)Se$_x$-rGO-CNT, some peaks, which were related to CoFe alloy, are observed. It might be attributed that there were nanocrystals

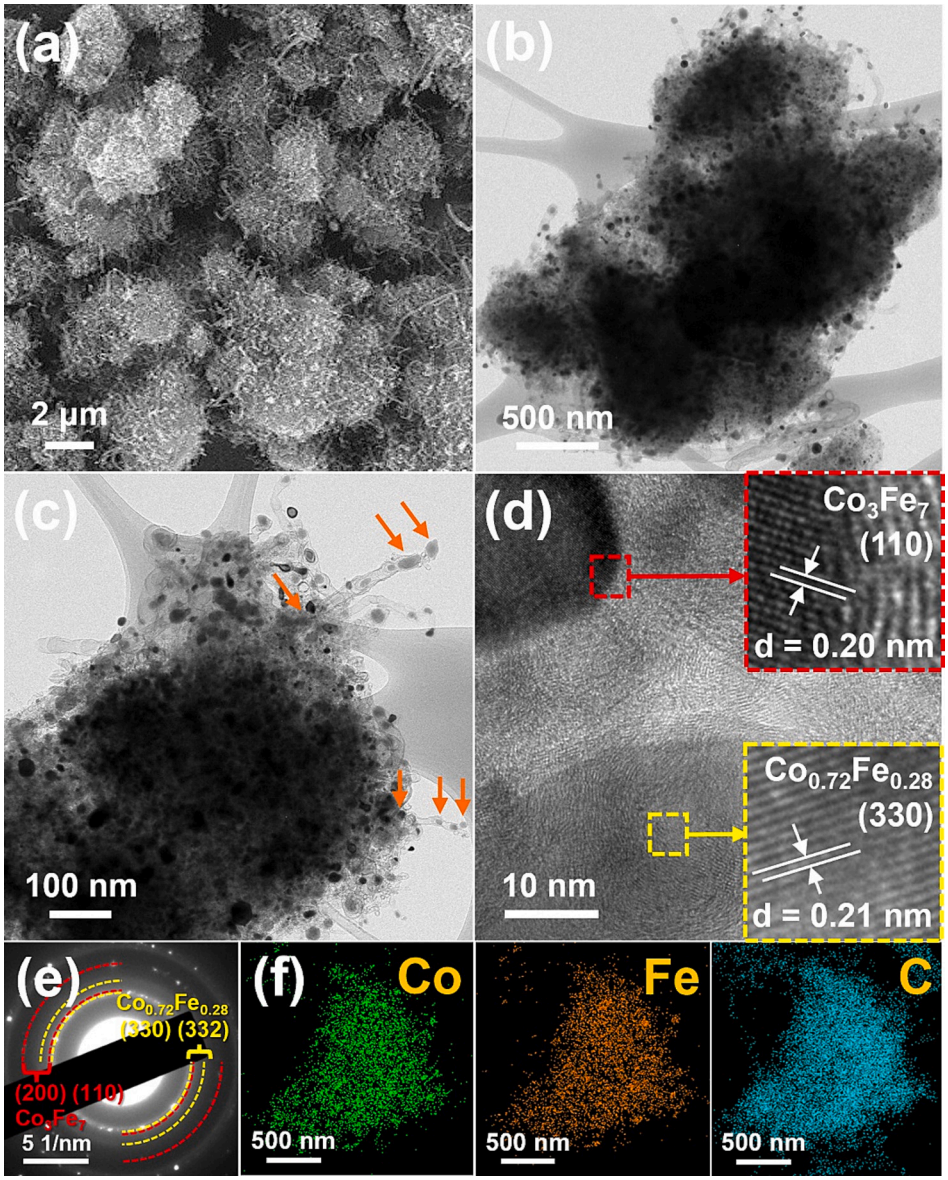

Fig. 1. Morphologies, SAED pattern and elemental mapping images of CoFe-rGO-CNT: (a) SEM image, (b, c) TEM images, (d) HR-TEM image, (e) SAED pattern and (f) elemental mapping images.

that were not completely selenized due to the influence of some thick graphitic carbon layers formed around CoFe alloy nanocrystal. In the case of the remaining CoFe alloy, it acts as a matrix to buffer volume changes during the conversion reactions of $CoSe_2$ and $FeSe_2$ with potassium ions [39–41]. Consequently, the presence of the remaining CoFe alloy improve the conductivity of the material and enhance the structural stability during the electrochemical conversion process. The compositions of (CoFe)Se_x-rGO-CNT were further studied by the X-ray photoelectron spectroscopy (XPS) spectra as shown in Fig. 4b–f. The Co 2p spectrum of (CoFe)Se_x-rGO-CNT shown in Fig. 4b exhibited Co $2p_{3/2}$ and Co $2p_{1/2}$ orbital peaks at 779.9 and 795.8 eV, respectively, confirming the typical formation of $CoSe_2$ phase [42]. The doublet peaks at 778.4 and 793.5 eV, which corresponded to Co $2p_{3/2}$ and Co $2p_{1/2}$ orbital peaks, respectively, indicated the presence of the metallic Co phase [43]. The Co $2p_{3/2}$ and Co $2p_{1/2}$ orbital peaks were additionally observed at 781.7 and 797.6 eV, respectively, indicating the presence of the oxidized cobalt selenite [44]. Corresponding satellite peaks were observed at around 785.7 and 803.4 eV. The Fe 2p spectrum of (CoFe)Se_x-rGO-CNT shown in Fig. 4c represented similar appearance compared to the Co 2p spectrum. The high-resolution Fe 2p spectrum was resolved into three pairs of doublets for metallic Fe (706.9/719.3 eV), $FeSe_2$ (707.2/720.2 eV), and selenite (710.6/712.9/723.7/725.9 eV), along with weak peaks from the satellites [45,46]. In the Se 3d spectrum in Fig. 4d, the binding energies of Se $3d_{5/2}$ and Se $3d_{3/2}$ at 54.8 and 55.7 eV, respectively, are also consistent with metal selenide ($CoSe_2$ and $FeSe_2$) [46,47]. The presence of peaks corresponding to the metal selenites indicated the formation of not only an (Co or Fe)-O bond but also a (Co or Fe)-Se bond in the metal-based selenides [48]. The N 1s spectrum, originating from N-doped CNT, as shown in Fig. 4e, was deconvoluted into four peaks at 398.2, 399.1, 400.7, and 403.8 eV, representing pyridinic N, pyrrolic N, graphitic N, and oxidized N, respectively [49]. The C 1s spectrum in Fig. 4f was divided into four peaks that were located at 284.6, 285.4, 286.1, and 287.1 eV, representing carbon-=carbon double bonding, carbon–N, carbon–O, carbon=O bonding, respectively [50]. The Raman spectra of CoFe-rGO-CNT, (CoFe)Se_x-rGO, (CoFe)Se_x-rGO-CNT commonly exhibited two clear peaks at 1352 and 1595 cm^{-1}, which correspond to the disordered (D-band) and graphitic features (G-band) in carbon, respectively. The value of I_D/I_G indicated the degree of graphitic disorder, and it could be used as an index to determine the degree of N doping or defects on the surface. The I_D/I_G

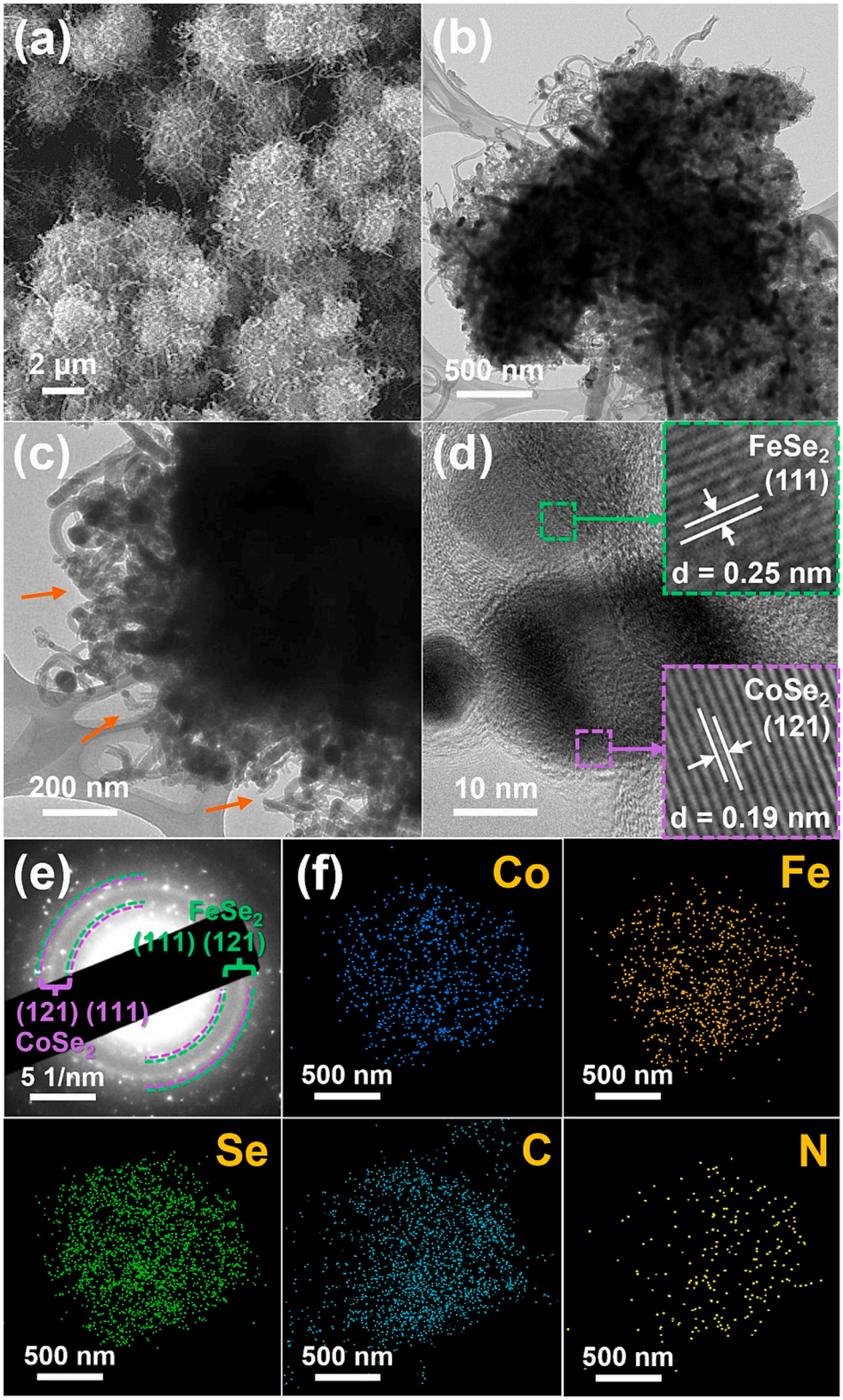

Fig. 2. Morphologies, SAED pattern and elemental mapping images of (CoFe)Se_x-rGO-CNT: (a) SEM image, (b, c) TEM images, (d) HR-TEM image, (e) SAED pattern and (f) elemental mapping images.

values of CoFe-rGO-CNT, (CoFe)Se_x-rGO-CNT were 1.03 and 1.01, respectively, which represented formation of N-doped CNT comparing to that 0.89 of (CoFe)Se_x-rGO. The specific surface areas and pore structures of (CoFe)Se_x-rGO-CNT and (CoFe)Se_x-rGO were analyzed by Brunauer–Emmett–Teller (BET) and Barrett–Joyner–Halenda (BJH) measurements. In the N_2 adsorption–desorption isotherms shown in Fig. S3, combinations of type-IV and H4 hysteresis loops were observed for the two samples, which indicate hierarchical mesoporous structures. However, the pore size distribution of two samples showed different trends. (CoFe)Se_x-rGO has developed mesopores between 10 and 100

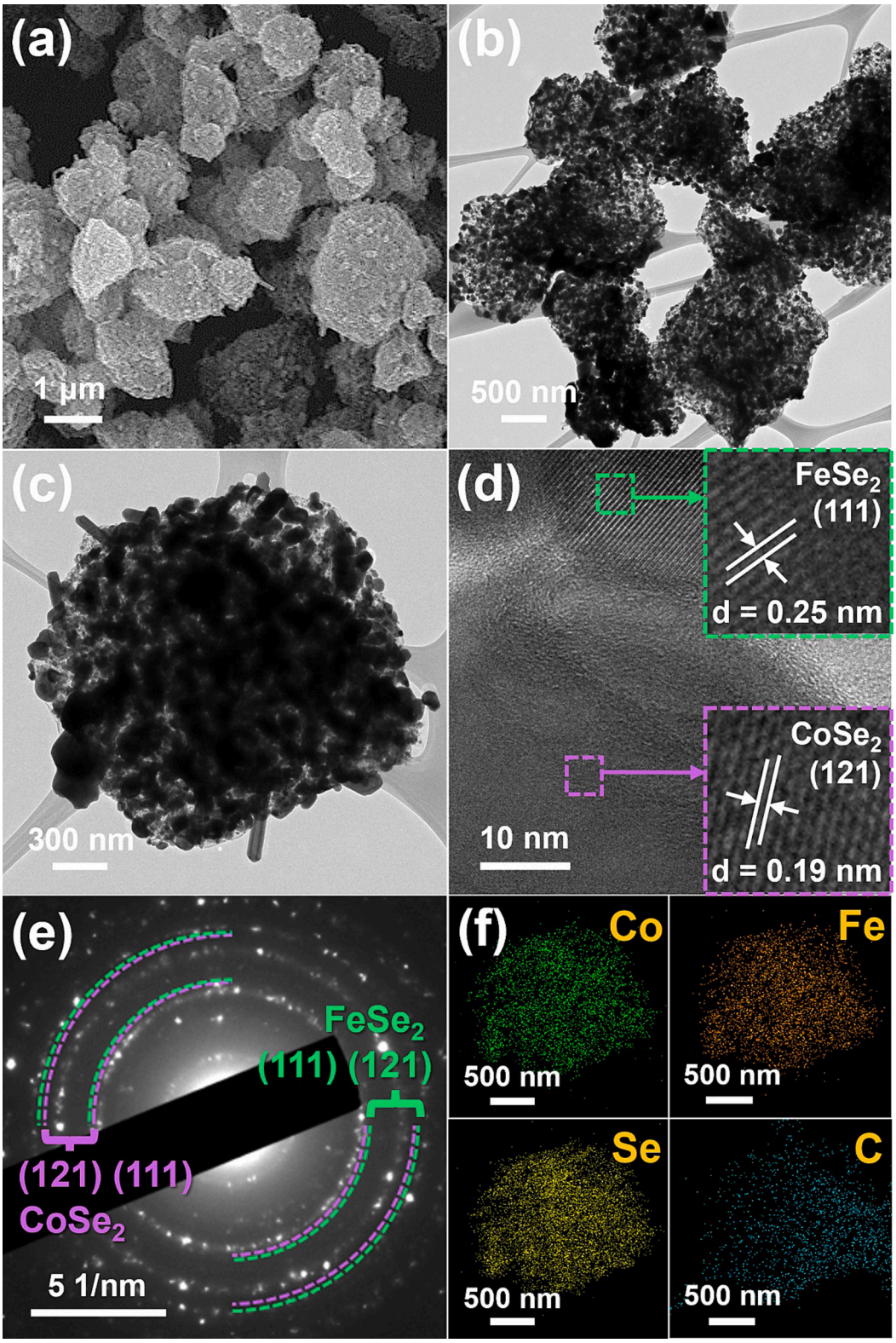

Fig. 3. Morphologies, SAED pattern and elemental mapping images of (CoFe)Se_x-rGO: (a) SEM image, (b, c) TEM images, (d) HR-TEM image, (e) SAED pattern and (f) elemental mapping images.

nm whereas (CoFe)Se_x-rGO-CNT has additionally developed 4 nm pores. It was comprehended that small mesopores were additionally generated as the CNT grew uniformly between the relatively large mesopores formed between the crumpled graphene sheets. The BET surface areas of (CoFe)Se_x-rGO-CNT and (CoFe)Se_x-rGO were 39.3 and 36.5 $m^2\ g^{-1}$, respectively. The thermogravimetric (TG) curves of (CoFe)Se_x-rGO-CNT and (CoFe)Se_x-rGO are depicted in Fig. S4. The XRD patterns of both samples after heat treatment at 800 °C under air condition, as shown in Fig. S5, matched well with the $CoFe_2O_4$ and Co_3O_4 phases. During the high-temperature heat treatment, phase separation of some Co occurred,

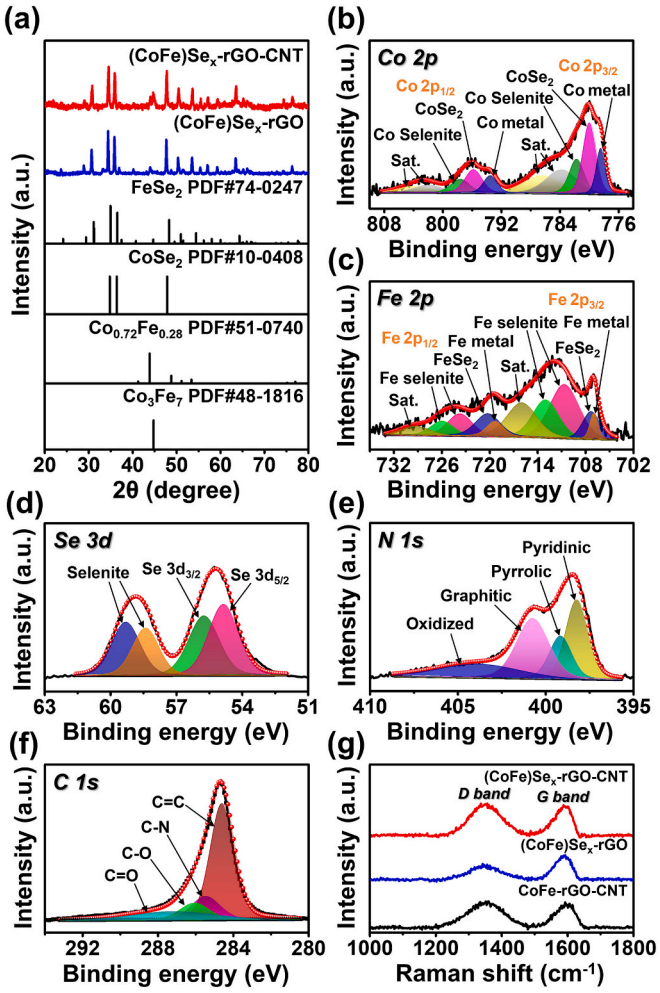

Fig. 4. (a) XRD patterns of (CoFe)Se$_x$-rGO-CNT and (CoFe)Se$_x$-rGO. High resolution XPS spectra of (CoFe)Se$_x$-rGO-CNT: (b) Co 2p, (c) Fe 2p, (d) Se 3d, (e) N 1s, and (f) C 1s. (g) Raman spectra.

leading to the additional observation of the Co_3O_4 phase. Furthermore, the down shifting of XRD peaks occurs due to the enhancements in lattice parameters caused by the larger ionic radius of Co^{2+} compared to Fe^{2+} [37,38]. The weight losses of (CoFe)Se$_x$-rGO-CNT and (CoFe)Se$_x$-rGO were 72 and 68 wt%. Derived from the TG curves, the carbon contents of both samples, starting from the same $(Co_{0.5}Fe_{0.5})Se_2$ phase, were calculated to be 57 and 50 wt%, respectively. Based on that (CoFe)Se$_x$-rGO-CNT and (CoFe)Se$_x$-rGO have the same weight ratio of (CoFe)Se$_x$, the carbon content of (CoFe)Se$_x$-rGO-CNT was composed of 43 % of rGO and 14 % of CNT.

3.2. Electrochemical performance

The electrochemical properties of (CoFe)Se$_x$-rGO-CNT and (CoFe)Se$_x$-rGO were evaluated using specific electrolyte types suitable for potassium-ion batteries. These two types of electrolytes were applied to electrodes, specifically potassium bis(fluorosulfonyl)imide (KFSI) in 1,2-dimethoxyethane (DME) and KFSI in the mixture of ethyl carbonate (EC) and diethyl carbonate (DEC) in a 1:1 volumetric ratio. The cyclic voltammetry (CV) analysis was performed at a scan rate of 0.1 mV s^{-1} over the potential range of 0.001–3.0 V for 5 cycles, as shown in Fig. 5. The CV tests of (CoFe)Se$_x$-rGO-CNT were conducted by two types of electrolytes and exhibited different cathodic and anodic peaks as shown in Fig. 5a and b. In using KFSI/DME electrolyte, three reduction peaks were observed at 0.96, 0.57, and 0.01 V, respectively. The first reduction at 0.96 V could be assigned to the formation of the K$_y$(CoFe)Se$_x$ phases and SEI layer by the K^+ intercalation into cobalt-iron selenide nanocrystals. The second reduction peak at 0.57 V was related to the conversion reaction of K$_y$(CoFe)Se$_x$ to metallic Co and Fe, and K$_y$Se$_x$ phases [48]. The last reduction peak near 0 V was attributed to the intercalation of K^+ into rGO and CNT component [51]. Therefore, the initial discharging reaction can be presented as follow:

$$(CoFe)Se_2 + xK^+ + xe^- \rightarrow K_x(CoFe)Se_2 \quad (1)$$

$$K_x(CoFe)Se_2 + (2-x)K^+ + (2-x)e^- \rightarrow CoFeSe + K_2Se \quad (2)$$

$$CoFeSe + 2K^+ + 2e^- \rightarrow Co + Fe + K_2Se \quad (3)$$

Four small anodic peaks were observed in subsequent initial charging process. The first anodic peak at 0.52 V was relevant to extraction of K^+ from rGO and CNT [52,53]. The oxidation peaks at 1.02

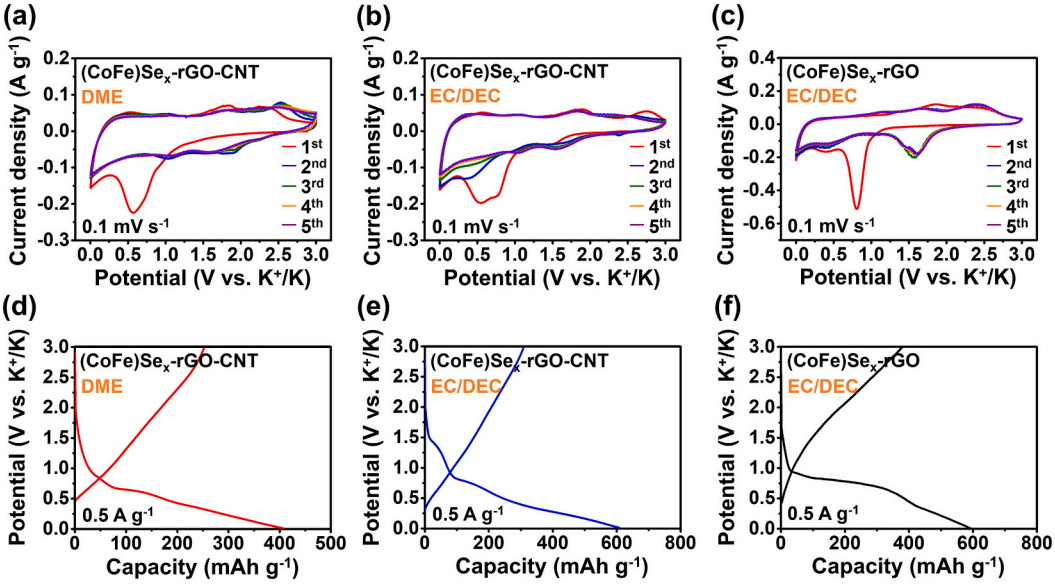

Fig. 5. (a–c) CV curves and (d–f) initial discharge and charge curves: (a, d) (CoFe)Se$_x$-rGO-CNT using DME electrolyte, (b, e) (CoFe)Se$_x$-rGO-CNT using EC/DEC electrolyte and (c, f) (CoFe)Se$_x$-rGO using EC/DEC electrolyte.

and 1.82 V were ascribed to formation of intermediate phases through conversion reactions. Subsequently, the peak at 2.35 V was attributed to the regeneration of $CoSe_2$ through a full conversion reaction, whereas the K_xFeSe_2 phase underwent further extraction of K^+ ions, instead of converting to $FeSe_2$ [54,55]. Thus, the subsequent charging process can be ascribed as follow [34,55,56]:

$$Co + Fe + 2K_2Se \rightarrow K_xCoSe_2 + K_xFeSe_2 + (4-x)K^+ + (4-x)e^- \quad (4)$$

$$K_xCoSe_2 \rightarrow CoSe_2 + xK^+ + xe^- \quad (5)$$

$$K_xFeSe_2 \rightarrow K_yFeSe_2 + (x-y)K^+ + (x-y)e^- (0 < y < x < 2) \quad (6)$$

After the initial cycle, solid-solution $(Co_{0.5}Fe_{0.5})Se_2$ divided into a heterointerfaced cobalt selenide and iron selenide nanocomposite, as reported at the previous literature [48]. On the other hand, the CV curves of (CoFe)Se_x-rGO-CNT applying to KFSI in EC/DEC showed peaks at 1.50, 0.77, 0.51, and 0.01 V. The additional peak at 1.5 V is associated with the initial intercalation of K^+ into (CoFe)Se_x-rGO-CNT electrode. The peak at 0.77 V is related to the formation of intermediate phases and the SEI layer, following the subsequent peak at 0.51 V is associated with the conversion reaction of intermediate phases to metallic Co and Fe, and K_ySe_x phases [54]. It is noteworthy that the potential of the initial cathodic peaks in the DME electrolyte (0.96 and 0.57 V) is higher than that in the EC/DEC electrolyte (0.77 and 0.51 V), respectively, which could be attributed to the more serious polarization in the EC/DEC electrolyte. During the oxidation process, the anodic peaks applied with DME electrolyte appeared at a slightly lower potential than that of EC/DEC. This further indicates the better reaction reversibility in the DME electrolyte. The possible reason can be the co-intercalation with solvated-K-ions in $(Co_{0.5}Fe_{0.5})Se_2$, which induced more occurrence of conversion reaction in the DME electrolyte system [57,58]. The CV curves of (CoFe)Se_x-rGO as a comparative sample were obtained applying to KFSI/EC/DEC electrolyte as shown in Fig. 5c. The overall cathodic and anodic peaks generally matched at the almost same potentials. The cathodic sharp peak at around 0.81 V in (CoFe)Se_x-rGO exceptionally was observed comparing to that of (CoFe)Se_x-rGO-CNT. Its reductive peak possibly was related to K^+ ion adsorption onto the surface-active site of cobalt iron selenide and carbon composite. It could be comprehended that (CoFe)Se_x-rGO had a larger active site for K^+ ion adsorption than that of (CoFe)Se_x-rGO-CNT resulting in sharp cathodic peaks [59]. The potential profiles at initial discharging and charging of (CoFe)Se_x-rGO-CNT and (CoFe)Se_x-rGO, using the specific electrolyte types, at current density of 0.5 A g^{-1} over a potential range of 0.001–3.0 V, were shown in Fig. 5d–f. The overall plateaus of the potential profiles were consistent with reduction and oxidation peaks observed in the CV curves well. The initial discharge and charge capacities of (CoFe)Se_x-rGO-CNT using DME based electrolyte were 407.4 and 253.6 mAh g^{-1}, respectively, resulting in a high initial Coulombic efficiency (ICE) of around 62.2 %. As a comparative sample, (CoFe)Se_x-rGO-CNT using EC/DEC based electrolyte exhibited a lower ICE of 51.1 %. The high ICE demonstrated the superiority of ether-based electrolytes. To investigate the phase transition of (CoFe)Se_x-rGO-CNT using DME based electrolyte during the initial discharging and charging processes, ex-situ XRD analysis was conducted using disassembled electrodes at pre-selected potentials, as shown in Fig. S6. The peaks observed at 45° across all potential ranges correspond to the Co_3Fe_7 (PDF#48-1816), indicating the presence of residual alloy in the (CoFe)Se_x-rGO-CNT materials. When discharging to 1.1 V, the diffraction peaks exhibited a similar tendency to the pristine (CoFe)Se_x-rGO-CNT, and new peaks appeared at 26.2° and 29.6°, corresponding to $KSeFO_3$ and $K_3(SO_4)F$ (PDF#89-0359), respectively [60]. These peaks are indicative of a side reaction between the KFSI/DME electrolyte and the electrode materials [61]. After discharging to 0.7 V, the main peaks of $CoSe_2$ (PDF#10-0408) and $FeSe_2$ (PDF#74-0247) disappear with the introduction of K^+. As a result, other diffraction peaks are observed at around 25.6°, 29°, and 30°, corresponding to the KO_2 (PDF#77-0211), $KFeSe_2$ and K_2CoSe_2 phase, respectively [62,63]. Moreover, a crystalline selenium peak may appear around 28°, suggesting the decomposition of unstable K_2Se into potassium and selenium [64]. At discharging to 0.4 V, there are no obvious characteristic changes signaled in the XRD patterns. Finally, at the fully discharged to 0.001 V, new peaks emerge, indicating the formation of the conversion reaction products, including K_2Se (JCPDS#23-0470) at 32° and 38°, as well as Fe_2O_3 (PDF#39-0238) at 33°. Additionally, peak of Co could be not observed, which might be attributed to its low crystallinity. During the subsequent charging to 0.5 V, new peaks are not observed, and the intensity of K_2Se diminishes due to the extraction of potassium. When charged to 1.1 V, the peaks of $KFeSe_2$ and K_2CoSe_2 were observed again. These products remain until the final charge state at 3.0 V. Consequently, this result presents that final charge product is K_xFeSe_2. Thereafter, the reversible reaction aligns with the interaction between K_xFeSe_2 and Fe as reported in a previous study [55]. However, in the case of $CoSe_2$, only portion of K_2CoSe_2 is observed as potassium ion cannot fully extract due to the low crystallinity. The results of the ex-situ XRD analysis were accorded well with the results of the CV analysis.

The in-situ electrochemical impedance spectroscopy (EIS) during the initial discharging and charging processes of (CoFe)Se_x-rGO-CNT and (CoFe)Se_x-rGO using the specific electrolyte types was explored at a current density of 0.1 A g^{-1} over the potential range of 0.001–3.0 V, as shown in Fig. 6. The equivalent circuit has been commonly used to fit EIS analysis, as indicated in Fig. 6a. In the fitted circuit, R_s is solution resistance, while R_{sei} and R_{ct} are the interfacial layer associated with the SEI and charge transfer resistance, respectively. Furthermore, CPE_{sei} and CPE_{dl} are the constant phase elements associated with the SEI capacitance and the electric double layer, while Z_w is the Warburg impedance. The Nyquist plots, which were measured at specific potentials during the initial discharging and charging processes, were collected and summarized in Fig. 6b, d and f. The variation of the total resistance ($R_{tot} = R_s + R_{sei} + R_{ct}$) during the initial cycle, obtained by in-situ EIS at predetermined potentials, was represented by the corresponding colored dots in Fig. 6c, e and g. The three cases, namely (CoFe)Se_x-rGO-CNT using DME based electrolyte, (CoFe)Se_x-rGO-CNT using EC/DEC based electrolyte, and (CoFe)Se_x-rGO using EC/DEC based electrolyte, commonly showed drastic decrease of R_{tot} values until 1.0 V, which was attributed to the aging of the potassium ion that initiated the initial potassiation process, regardless of the sufficient aging time (6 h). In all three tests, the transformation of large (CoFe)Se_x crystals into ultrafine metallic cobalt and iron nanocrystals by electrochemical conversion reaction as well as formation of SEI layers occurred, which contributed to a continuous decrease in R_{tot} until discharging end [65]. Among these cases, the largest reduction in resistance was observed in (CoFe)Se_x-rGO-CNT using DME based electrolyte. The co-intercalation with solvated-K-ions in $(Co_{0.5}Fe_{0.5})Se_2$ induced more occurrence of conversion reaction in the DME electrolyte system. In addition, uniformity of the thin SEI layer from DME electrolyte significantly affected decrease of resistance as reported the previous literatures [57,58]. During the charging process, both (CoFe)Se_x-rGO-CNT and (CoFe)Se_x-rGO using EC/DEC based electrolyte exhibited increase of R_{tot} values until 2.0 V. It was attributed to the structural strain induced by the stepwise formation of (CoFe)Se_x. However, the volume contraction arising from the depotassiation and partial dissolution of the SEI layer contributed to the decrease in resistance until the fully charged state [65]. The small (CoFe)Se_x nanocrystal surrounded graphitic carbon and developed CNT matrix of (CoFe)Se_x-rGO-CNT contributed to the lower resistance compared to (CoFe)Se_x-rGO at end of the charging. On the other hand, (CoFe)Se_x-rGO-CNT using DME based electrolyte maintained a constant R_{tot} value without a large change in resistance until charging was completed. The stable SEI layer and co-intercalation with solvated-K-ions in $(Co_{0.5}Fe_{0.5})Se_2$ and the hierarchically grown N-doped CNT collectively contributed to a low resistance of electrode during the cycle. The in-situ EIS during the second discharging and charging process of (CoFe)Se_x-rGO-CNT electrode using DME based electrolyte was presented in Fig. S7. The overall R_{tot} value during the second cycle exhibited lower resistance than in the

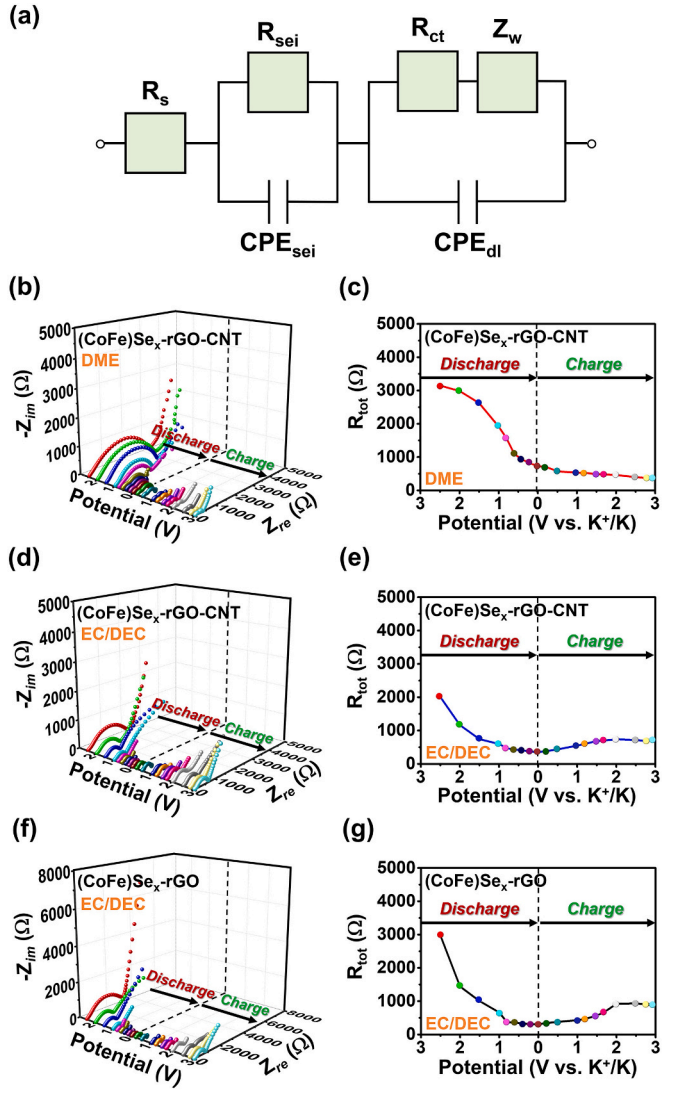

Fig. 6. (a) Equivalent circuit cell diagram of EIS, (b, d, f) in-situ Nyquist plots and (c, e, g) R_{tot} vs. potential graphs of (b, c) (CoFe)Se_x-rGO-CNT using DME electrolyte, (d, e) (CoFe)Se_x-rGO-CNT using EC/DEC electrolyte and (f, g) (CoFe)Se_x-rGO using EC/DEC electrolyte during the initial cycle. (For interpretation of the references to color in this figure, the reader is referred to the web version of this article.)

initial cycle, attributed to the ultrafine cobalt and iron selenide nanocomposite divided from the solid-solution (CoFe)Se_2 [66]. During the second discharging process, the R_{tot} value continued to increase until 0.001 V. This suggested that the formation of metallic cobalt and iron nanocrystals, along with the volume expansions resulting from the insertion of potassium ions into cobalt and iron selenide nanocomposites and carbon components, influenced the increase in resistance. Furthermore, the large variation in resistance value at low voltage regions demonstrated that the intercalation/deintercalation of potassium ions into the carbon structure has a more pronounced influence than into ultrafine cobalt and iron selenide [67]. During the second charging process, R_{tot} value decreased until 3.0 V, which is attributed to volume contraction and formation of ultrafine cobalt and iron selenide nanocomposite due to the depotassiation. These reactions are in good agreement with the CV curves and ex-situ XRD analysis data. According to these results, the reversible electrochemical reaction in the second discharging/charging process can be presented as follow [55,68–70]:

$$CoSe_2 + 4K^+ + 4e^- \leftrightarrow Co + 2K_2Se \quad (7)$$

$$K_xFeSe_2 + (4-x)K^+ + (4-x)e^- \leftrightarrow Fe + 2K_2Se \quad (8)$$

The cycle performances of three electrodes measured at a current density of 0.2 A g^{-1} were compared and exhibited in Fig. 7a. These electrodes showed different capacity variations during the repeated 100 cycles. As confirmed by TG analysis in Fig. S4, (CoFe)Se_x-rGO contained a lower amount of carbon content in the total cobalt-iron selenide-C composite than that of (CoFe)Se_x-rGO-CNT. The carbon component containing rGO and CNT, which exercise capacities by intercalation-deintercalation mechanism of potassium ions, exhibited lower reversible capacities comparing to cobalt-iron selenide component, which exerted capacities by conversion mechanism with potassium ions. In this regard, (CoFe)Se_x-rGO electrode using EC/DEC based electrolyte showed larger reversible capacities during the initial 50 cycles relative to those of (CoFe)Se_x-rGO-CNT using DME and EC/DEC based electrolytes. However, the Coulombic efficiencies of (CoFe)Se_x-rGO electrode rapidly decreased after the 20th cycle, which was attributed to structural instability caused by the large cobalt-iron selenide nanocrystals over the rGO layers, as well as the formation of thick SEI layer. As a result, (CoFe)Se_x-rGO electrode exhibited a sharp capacities decay in capacity to 170.1 mAh g^{-1} after 40 cycles. In contrast, (CoFe)Se_x-rGO-CNT electrode under same EC/DEC based electrolytes displayed lower reversible capacities than that of (CoFe)Se_x-rGO electrode until the 60th cycle, while maintaining a stable cycle performance and reversing its capacities after the 60th cycle. Cobalt-iron selenide nanocrystals surrounded by graphitic carbon layer and porous rGO-CNT composite architecture contributed to structural stability during the repeated potassiation and depotassiation process [71]. As shown in Table S1, the structure stability of rGO-CNT template with bimetallic selenide enables stable cycling and rate properties compared to previously reported graphene and CNT based anode materials for potassium-ion batteries. On the other hand, (CoFe)Se_x-rGO-CNT electrode using DME based electrolyte demonstrated continuous capacities increase up to the 60th cycle, which was attributed to more occurrence of conversion reaction within the DME electrolyte system by co-intercalation with solvated-K-ions in $(Co_{0.5}Fe_{0.5})Se_2$. Moreover, the synergistic effect of thin SEI layer and structural advantages of the electrode facilitated excellent retention of Coulombic efficiencies and outstanding cycle performance maintaining high reversible capacities. The contribution of the rGO-CNT component to the capacities of (CoFe)Se_x-rGO-CNT for potassium-ion storage was investigated. For this purpose, CoFe-rGO-CNT was immersed in strong nitric acid during the overnight resulting in the formation of rGO-CNT by etching metallic cobalt-iron alloys. rGO-CNT electrode had a similar hierarchical morphology to (CoFe)Se_x-rGO-CNT, as shown in Fig. S8. Some cobalt-iron crystals remained despite being etched in strong nitric acid as shown in XRD data (Fig. S9). The cobalt-iron nanocrystal surrounded by a thick graphitic carbon layer was not easily etched, and this is the same result as the metallic CoFe alloy nanocrystal remaining without being completely selenized in (CoFe)Se_x-rGO-CNT. The discharge capacity of rGO-CNT at a current density of 0.2 A g^{-1} for the 100th cycle was 231.8 mAh g^{-1} (Fig. S10). Therefore, the contribution of rGO-CNT to the discharge capacity of (CoFe)Se_x-rGO-CNT could be estimated as being 28.2 %. To confirm the capacity contribution of rGO-CNT, only rGO and CNT were synthesized, and their SEM images and electrochemical performances were presented in Fig. S11. The discharge capacities of only rGO and CNT using DME electrolytes at a current density of 0.2 A g^{-1} for the 60th cycle were 73.1 and 256.1 mAh g^{-1}. Considering that the carbon content of (CoFe)Se_x-rGO-CNT was composed of 43 % of rGO and 14 % of CNT, the contribution of rGO and CNT to the discharge capacity of (CoFe)Se_x-rGO-CNT could be estimated as 6.6 and 7.5 %, respectively. The rate performances of (CoFe)Se_x-rGO-CNT and (CoFe)Se_x-rGO as the specific electrolyte type are measured at increasing rates from 0.2 to 5.0 A g^{-1} and shown in Fig. 7b. As confirmed by cycle performance in Fig. 7a, (CoFe)Se_x-rGO electrode showed higher capacities during c-rate tests, but the rate of capacities decrease with increasing current densities was the highest

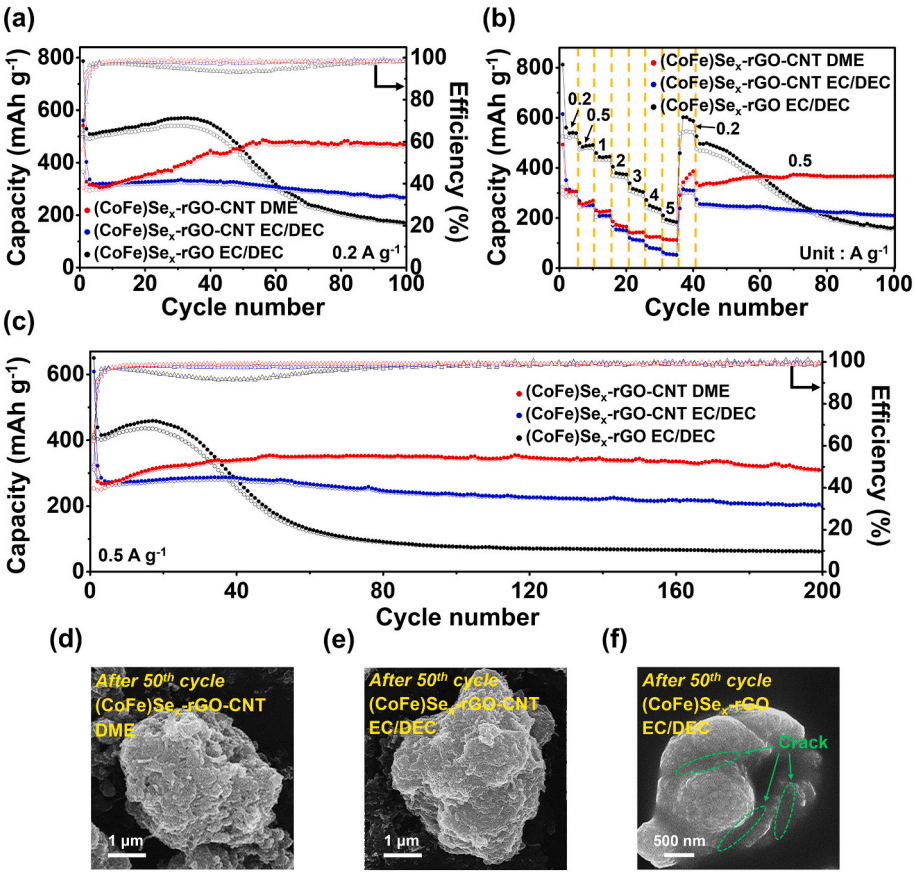

Fig. 7. Electrochemical properties of (CoFe)Se_x-rGO-CNT using DME and EC/DEC electrolytes and (CoFe)Se_x-rGO using EC/DEC electrolyte: (a) cycle performances at a current density of 0.2 A g^{-1}, (b) rate performances, and (c) long-term cycle performances at current density of 0.5 A g^{-1}. SEM images after 50th cycle of (d) (CoFe)Se_x-rGO-CNT using DME electrolyte, (e) (CoFe)Se_x-rGO-CNT using EC/DEC electrolyte and (f) (CoFe)Se_x-rGO using EC/DEC electrolyte.

compared to (CoFe)Se_x-rGO-CNT electrodes. The large cobalt-iron selenide nanocrystals of (CoFe)Se_x-rGO and structural instability contributed to poor rate capabilities. On the other hand, (CoFe)Se_x-rGO-CNT electrode using DME based electrolyte demonstrated excellent rate capabilities comparing to electrode using EC/DEC based electrolyte. The synergistic effect of porous architecture, high conductive N-doped CNT and thin SEI layer applied to the DME electrolyte facilitated the enhanced rate capabilities. (CoFe)Se_x-rGO-CNT electrodes using DME based electrolytes exhibited reversible discharge capacities of 344.7, 261.3, 227.2, 170.3, 142.2, 125.1, and 113.8 mAh g^{-1} at current densities of 0.2, 0.5, 1.0, 2.0, 3.0, 4.0, and 5.0 A g^{-1}, respectively. Moreover, they showed stable reversible capacity recovery at a low current density of 0.2 A g^{-1}. The rate performances of (CoFe)Se_x-rGO-CNT with the active materials mass loadings of 0.82, 1.46, and 2.01 mg cm^{-2}, prepared by using doctor blades set at 15, 20, and 30 μm, respectively, are shown in Fig. S12. In terms of areal capacities, at a mass loading of 2.01 mg cm^{-2}, a predominant decrease in capacity retention was observed at higher current density. Furthermore, a mass loading of 0.82 mg cm^{-2} exhibited stable capacity retention compared to a mass loading of 1.46 mg cm^{-2}. Similarly, in weight specific capacities, mass loading of 0.82 and 1.46 mg cm^{-2} demonstrated comparable levels of capacity retention. The electrode with different mass loadings can exhibit variations in capacity not only due to thickness effect but also distinct internal resistances based on electrode density and porosity [72]. The high loading test exhibited that the electrode maintained stable rate performance even with an increase in mass loading to a certain level. The cycling tests at a current density of 0.5 A g^{-1}, evaluated following the rate test, were continuously conducted, and are shown in Fig. 7b. Afterwards, up to the 100th cycle, (CoFe)Se_x-rGO showed a continuous capacity decrease, whereas (CoFe)Se_x-rGO-CNT electrodes using DME and EC/DEC based electrolytes demonstrated stable cycle characteristics. The long-term cycle performances of three electrodes additionally were carried out at a current density of 0.5 A g^{-1} and are shown in Fig. 7c. (CoFe)Se_x-rGO-CNT electrode, using DME based electrolyte, exhibited a discharge capacity of 309.8 mAh g^{-1} with high CEs (>99.3 %), whereas (CoFe)Se_x-rGO-CNT and (CoFe)Se_x-rGO electrodes using EC/DEC based electrolytes had low discharge capacities of 199.2 and 61.8 mAh g^{-1} after 200 cycles, respectively. As shown in Table S2, the electrochemical performance of (CoFe)Se_x-rGO-CNT using DME based electrolyte has indicated improvement compared to previously reported selenide-based anode materials for potassium-ion batteries. These advantages are based on the higher structural stability and thin SEI layer of (CoFe)Se_x-rGO-CNT using DME based electrolyte. The thin SEI layer was formed due to the less solvent decomposition, which can be explained by the energy disparity between the lowest unoccupied molecular orbital (LUMO) and highest occupied molecular orbital (HOMO) level of KFSI, EC/DEC and DME. As reported in previous literature [73], among KFSI, EC, DEC and DME, DME displayed the highest LUMO level, while the others showed similar levels. In the case of KFSI/DME electrolyte, during the initial cycle, KFSI was preferentially decomposed, forming a thin SEI layer consisting of inorganic components. On the other hand, in the case of KFSI in EC/DEC electrolyte, both KFSI and EC/DEC were simultaneously decomposed, resulting in the formation of a thick SEI layer composed of a mixture of inorganic/organic components [58,74]. These results matched well with the SEM images obtained after 50 cycles in Fig. 7d–f.

To evaluate the potassium ion diffusion behavior during charging and discharging of the electrodes, the galvanostatic intermittent titration technique (GITT) analysis was conducted at the initial cycle as shown in Fig. 8. The GITT analysis was tested at a current density of 0.1 A g^{-1}, with pulse time 20 min and relaxation time 60 min and their

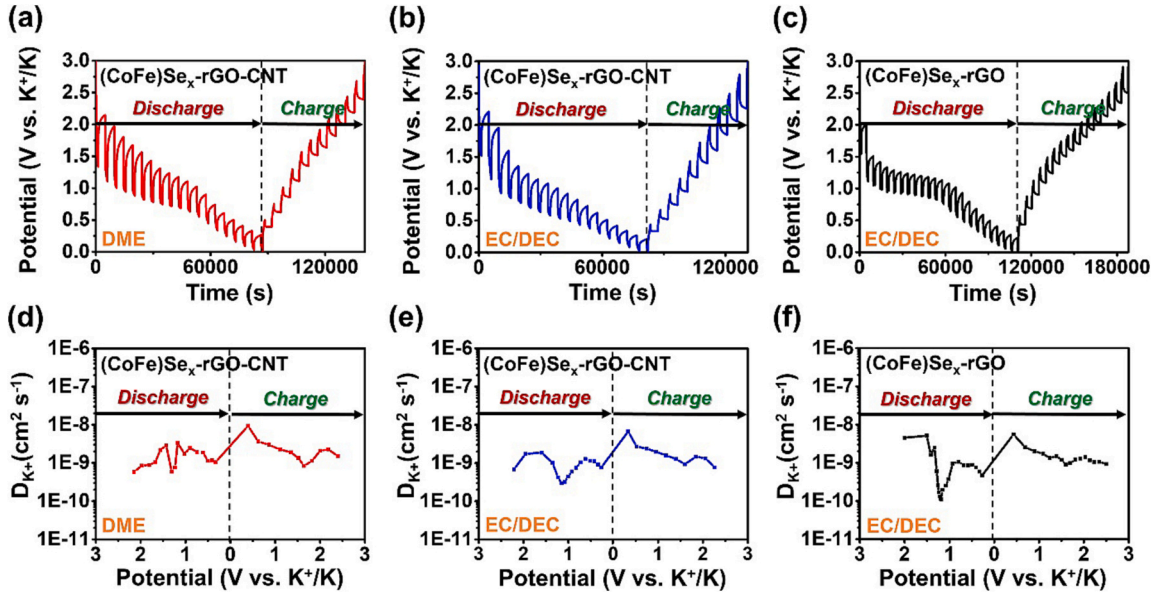

Fig. 8. GITT potential profiles and K^+-ion diffusion coefficients of (a, d) (CoFe)Se_x-rGO-CNT using DME electrolyte, (b, e) (CoFe)Se_x-rGO-CNT using EC/DEC electrolyte, (c, f) (CoFe)Se_x-rGO using EC/DEC electrolyte during the initial cycle.

profiles were shown in Fig. 8a–c. The potassium ion diffusion coefficient (denoted as D_{K+}) can be obtained using the following equation:

$$D_{K+} = 4 \Big/ \pi\tau \, (m_B V_M / M_B S)^2 \cdot (\Delta E_s / \Delta E_\tau)^2 \quad (9)$$

The relevant parameter values have been documented in previous studies [75]. Three electrodes commonly showed drastic decrease of D_{K+} value around 1.0 V during the discharging process as shown in Fig. 8d–f. The phase transition by conversion reaction and formation of SEI layer influenced obstruction of K^+ diffusion. At this time, the stable and thin SEI layer, which was derived from decomposition of DME based electrolyte, in (CoFe)Se_x-rGO-CNT electrode allowed a relatively small rate of decrease in D_{K+} value compared to electrodes using EC/DEC based electrolyte. During the charging process, phase transition to heterointerfaced cobalt selenide and iron selenide by oxidation process contributed to decrease of D_{K+} value until around 1.5 V. On the other hand, the volume contraction arising from the depotassiation and partial dissolution of the SEI layer contributed to the increase in D_{K+} value around 2.0 V. (CoFe)Se_x-rGO-CNT electrode using DME based electrolyte was observed to have a slightly higher average diffusion coefficient than (CoFe)Se_x-rGO-CNT and (CoFe)Se_x-rGO using EC/DEC based electrolytes, demonstrating the structural superiority of the uniformly distributed N-doped CNT and small cobalt-iron selenide nanocrystals and stable SEI layers in terms of enhanced electrochemical performance.

To understand and compare the reaction kinetics of the K^+ ion storage of three electrodes, CV-rate measurements were conducted at various scan rates of 0.1, 0.2, 0.4, 0.6, 0.8, 1.0 and 1.5 mV s^{-1} to confirm the capacity contribution during potassiation and depotassiation, as shown in Fig. 9. The CV curves of the three electrodes were commonly broadened and slightly shifted as the scan rate increased, which revealed the polarization of the electrodes. The capacitive contribution can be quantitatively analyzed using the following equation:

$$log(i) = blog(v) + log(a) \quad (10)$$

where i is the measured current and v is the scan rate [76]. The slope of the log(i) versus log(v) plot indicated the charge storage kinetics in the electrode. The calculated b values of (CoFe)Se_x-rGO-CNT using DME based electrolyte, (CoFe)Se_x-rGO-CNT and (CoFe)Se_x-rGO using EC/DEC based electrolytes at the cathodic/anodic peaks are 0.75/0.86, 0.75/0.85, and 0.63/0.80, respectively. These b values revealed that (CoFe)Se_x-rGO-CNT using DME based electrolyte had favorable capacitive kinetics [77]. As shown in Fig. 8, a higher slope in (CoFe)Se_x-rGO-CNT electrode using DME based electrolyte expressed a higher apparent K^+ ion diffusion coefficient. In words, both of GITT and CV results revealed that the DME electrolytes provided better kinetics including charge-transfer rates and K^+ ion diffusion rates. To confirm the pseudocapacitive and diffusion-controlled process contribution to the total capacity, the following equation was applied:

$$i(V) = k_1 v + k_2 v^{1/2} \quad (11)$$

where $k_1 v$ and $k_2 v^{1/2}$ correspond to the surface capacitive behavior and diffusion-controlled process, respectively [78]. The electrode dominated by the pseudocapacitive process exhibits superior rate performance owing to the rapid redox reaction at the surface. On the other hand, the electrode dominated by the diffusion-controlled process demonstrated stable electrochemical properties as ions intercalated into the interior of materials. At a scan rate of 1.5 mV s^{-1}, the capacitive contributions (indicated by the green color shaded area) of (CoFe)Se_x-rGO-CNT using DME based electrolyte, (CoFe)Se_x-rGO-CNT and (CoFe)Se_x-rGO using EC/DEC based electrolytes were 80, 79, and 72 %. The high ion mobility in terms of charge-transfer and diffusivity in the interlayer space by stable SEI layer and co-intercalation with solvated-K-ions in ($Co_{0.5}Fe_{0.5}$)Se_2 guaranteed a faster ion-exchange reaction. The capacitive contributions value of (CoFe)Se_x-rGO-CNT using DME based electrolyte continuously increased with the scan rate, reaching 80 % at a high scan rate of 1.5 mV s^{-1}, as shown in Fig. 9j. The ratio of the capacitive-controlled contribution of (CoFe)Se_x-rGO-CNT revealed a fast transport of the K^+ ions; this property improved the electrode rate capability.

As shown in Fig. S13, a full cell was fabricated using (CoFe)Se_x-rGO-CNT anode and Prussian blue (PB) cathode to verify the practical application of (CoFe)Se_x-rGO-CNT composite. PB was synthesized via co-precipitation and exhibited irregular morphological features, as confirmed by the SEM image in Fig. S13a. Additionally, the XRD pattern of potassium Prussian blue (KPB) matched well with $Fe_4[Fe(CN)_6]_3$, and as reported in the previously literature, the XRD peaks of $Fe_4[Fe(CN)_6]_3$ were almost identical to those of KPB (Fig. S13b) [79]. The initial charge and discharge curves of the PB cathode are shown in Fig. S13c, measured at a current density of 0.05 A g^{-1} within the voltage range of 2.0–4.0 V. Additionally, the cycle performance of the PB cathode showed a capacity of 60.1 mAh g^{-1} after 100 cycles at a current density of 0.05 A g^{-1}

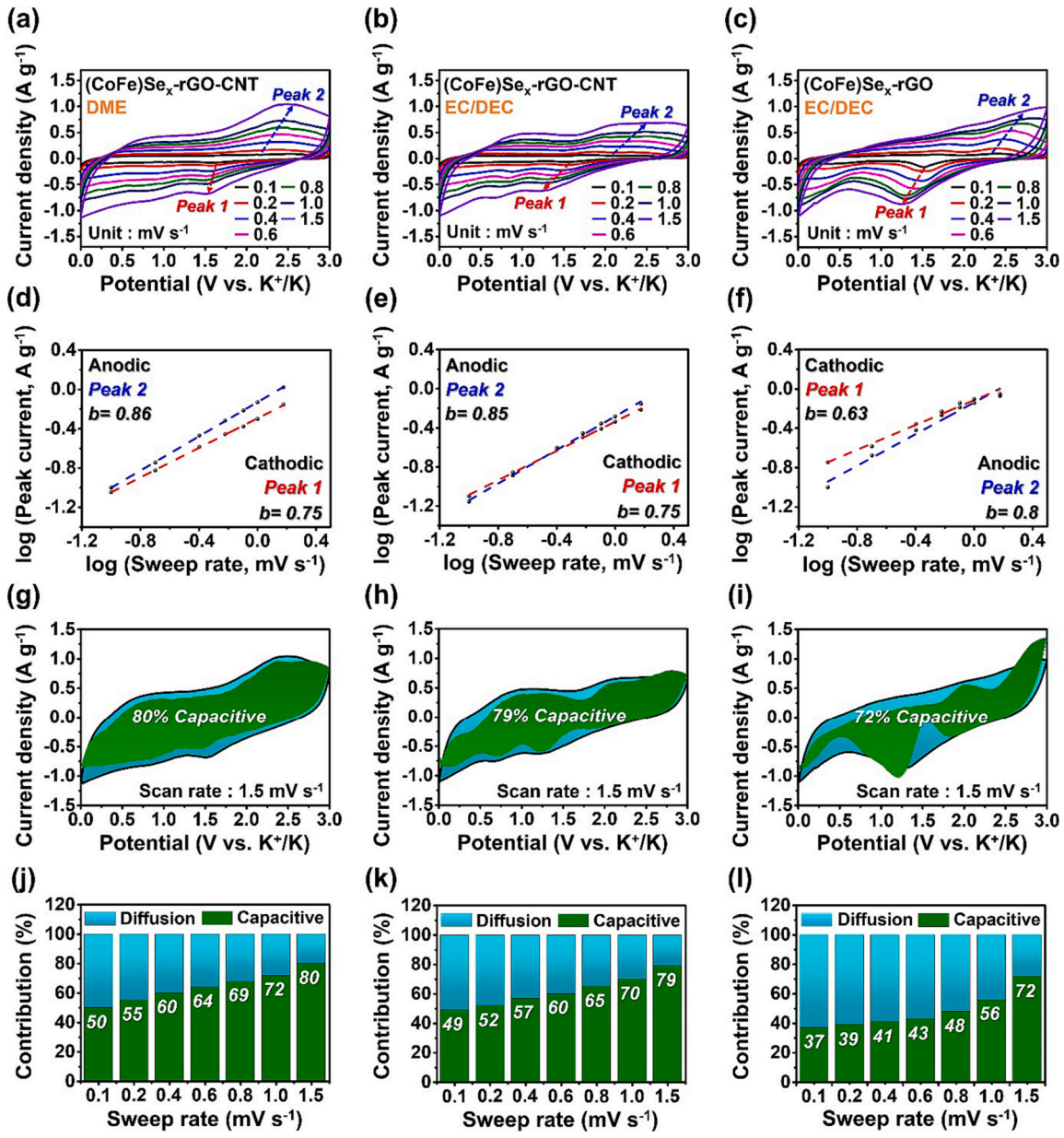

Fig. 9. CV curves at various sweep rates, fitted log (peak current) vs. log (scan rate) of peak 1 and peak 2, CV curves showing capacitive contribution (green color area) to the total current at a scan rate of 1.5 mV s^{-1} and capacitive contributions: (a, d, g, j) (CoFe)Se_x-rGO-CNT using DME electrolyte, (b, e, h, k) (CoFe)Se_x-rGO-CNT using EC/DEC electrolyte and (c, f, i, l) (CoFe)Se_x-rGO using EC/DEC electrolyte. (For interpretation of the references to color in this figure legend, the reader is referred to the web version of this article.)

(Fig. S13d). In the full cell test, the initial charge and discharge curves of the PB and (CoFe)Se_x-rGO-CNT full cell exhibited high capacities of 359.92 and 107.12 mA h g^{-1}, respectively, resulting in the initial CE of 30 % within a voltage range of 1.0–3.8 V at a current density of 0.1 A g^{-1} (Fig. S13e). After 30 cycles, the full cell showed a capacity of 225.1 mAh g^{-1} with CE of 90 % (Fig. S13f). Throughout cycling, the full cell consistently demonstrated superior capacity, CE, and stable cycling performance, validating its potential for practical applications.

4. Conclusions

In summary, for the first time, we propose (CoFe)Se_x-rGO-CNT composite microsphere as anode for potassium ion batteries, using spray pyrolysis and CVD process. This proposal effectively mitigated the stacking of graphene and facilitated the uniformly growth of CNTs on the rGO surface, forming a structurally stable template that prevented the formation of large bimetallic selenide during selenization. The rGO-CNT template minimized volume variation caused by K^+ intercalation-deintercalation compared to graphite, and the introduction of cobalt-iron selenide further enabled improved electrochemical performance. (CoFe)Se_x-rGO-CNT, which featuring a stable structure, exhibited superior Coulombic efficiency, cycle stability, rate capability and K^+ ion diffusion compared to (CoFe)Se_x-rGO. Moreover, (CoFe)Se_x-rGO-CNT exhibited enhanced performance when using DME electrolyte, which capable of forming a stable and thin SEI layer, compared to utilizing EC/DEC electrolyte. As a result, this study introduces an effectively strategy that involves inhibiting graphene stacking, applying appropriate electrolytes and employing bimetallic selenide anode for advanced potassium ion batteries.

CRediT authorship contribution statement

Sang-Hyun Kim: Writing – original draft, Formal analysis, Data curation. **Tae Ha Kim:** Writing – original draft, Formal analysis, Data curation. **Hyeon Ki Park:** Formal analysis, Conceptualization. **Yun Chan Kang:** Writing – review & editing, Conceptualization. **Jung Sang Cho:** Writing – review & editing, Conceptualization. **Gi Dae Park:** Writing – review & editing, Writing – original draft, Supervision, Conceptualization.

Declaration of competing interest

The authors declare that they have no known competing financial interests or personal relationships that could have appeared to influence the work reported in this paper.

Data availability

No data was used for the research described in the article.

Acknowledgments

This work was supported by a National Research Foundation of Korea (NRF) grant funded by the Korea government (MEST) (NRF-2022R1F1A1070886). This work was supported by the National Research Foundation of Korea (NRF) and the Commercialization Promotion Agency for R&D Outcomes (COMPA) funded by the Ministry of Science and ICT, South Korea (Grant No.: RS-2023-00217581, RS-2023-00304768).

Appendix A. Supplementary data

Supplementary data to this article can be found online at https://doi.org/10.1016/j.est.2024.110683.

References

[1] S.-H. Lee, V. Sridhar, J.-H. Jung, K. Karthikeyan, Y.-S. Lee, R. Mukherjee, N. Koratkar, I.-K. Oh, Graphene–nanotube–iron hierarchical nanostructure as lithium ion battery anode, ACS Nano 7 (2013) 4242–4251, https://doi.org/10.1021/nn4007253.

[2] D.G. Papageorgiou, I.A. Kinloch, R.J. Young, Mechanical properties of graphene and graphene-based nanocomposites, Prog. Mater. Sci. 90 (2017) 75–127, https://doi.org/10.1016/j.pmatsci.2017.07.004.

[3] A.A. Balandin, Thermal properties of graphene and nanostructured carbon materials, Nat. Mater. 10 (2011) 569–581, https://doi.org/10.1038/nmat3064.

[4] J. Balamurugan, T.D. Thanh, N.H. Kim, J.H. Lee, Facile synthesis of 3D hierarchical N-doped graphene nanosheet/cobalt encapsulated carbon nanotubes for high energy density asymmetric supercapacitors, J. Mater. Chem. A 4 (2016) 9555–9565, https://doi.org/10.1039/C6TA03132C.

[5] S. Peng, L. Li, X. Han, W. Sun, M. Srinivasan, S.G. Mhaisalkar, F. Cheng, Q. Yan, J. Chen, S. Ramakrishna, Cobalt sulfide nanosheet/graphene/carbon nanotube nanocomposites as flexible electrodes for hydrogen evolution, Angew. Chem. 126 (2014) 12802–12807, https://doi.org/10.1002/ange.201408876.

[6] S. Stankovich, D.A. Dikin, R.D. Piner, K.A. Kohlhaas, A. Kleinhammes, Y. Jia, Y. Wu, S.T. Nguyen, R.S. Ruoff, Synthesis of graphene-based nanosheets via chemical reduction of exfoliated graphite oxide, Carbon 45 (2007) 1558–1565, https://doi.org/10.1016/j.carbon.2007.02.034.

[7] C. Tang, Q. Zhang, M.Q. Zhao, J.Q. Huang, X.B. Cheng, G.L. Tian, H.J. Peng, F. Wei, Nitrogen-doped aligned carbon nanotube/graphene sandwiches: facile catalytic growth on bifunctional natural catalysts and their applications as scaffolds for high-rate lithium-sulfur batteries, Adv. Mater. 26 (2014) 6100–6105, https://doi.org/10.1002/adma.201401243.

[8] B. Yuan, Y. Shi, X. Mu, J. Wang, W. Xing, K.M. Liew, Y. Hu, A facile method to prepare reduced graphene oxide with a large pore volume, Mater. Lett. 162 (2016) 154–156, https://doi.org/10.1016/j.matlet.2015.10.011.

[9] S. Park, Y. Shao, H. Wan, P.C. Rieke, V.V. Viswanathan, S.A. Towne, L.V. Saraf, J. Liu, Y. Lin, Y. Wang, Design of graphene sheets-supported Pt catalyst layer in PEM fuel cells, Electrochem. Commun. 13 (2011) 258–261, https://doi.org/10.1016/j.elecom.2010.12.028.

[10] K.M. Subhedar, I. Sharma, S.R. Dhakate, Control of layer stacking in CVD graphene under quasi-static condition, Phys. Chem. Chem. Phys. 17 (2015) 22304–22310, https://doi.org/10.1039/C5CP03541D.

[11] X. Li, Z. Pan, Z. Li, X. Wang, B. Saravanakumar, Y. Zhong, L. Xing, M. Xu, C. Guo, W. Li, Coral-like reduced graphene oxide/tungsten sulfide hybrid as a cathode host of high performance lithium-sulfur battery, J. Power Sources 420 (2019) 22–28, https://doi.org/10.1016/j.jpowsour.2019.02.089.

[12] G. Gao, H.B. Wu, X.W. Lou, Citrate-assisted growth of $NiCo_2O_4$ nanosheets on reduced graphene oxide for highly reversible lithium storage, Adv. Energy Mater. 4 (2014) 1400422, https://doi.org/10.1002/aenm.201400422.

[13] I. Shakir, High energy density based flexible electrochemical supercapacitors from layer-by-layer assembled multiwall carbon nanotubes and graphene, Electrochim. Acta 129 (2014) 396–400, https://doi.org/10.1016/j.electacta.2014.02.124.

[14] I. Shakir, Z. Ali, J. Bae, J. Park, D.J. Kang, Layer by layer assembly of ultrathin V_2O_5 anchored MWCNTs and graphene on textile fabrics for fabrication of high energy density flexible supercapacitor electrodes, Nanoscale 6 (2014) 4125–4130, https://doi.org/10.1039/C3NR06820J.

[15] T.-T. Chen, W.-L. Song, L.-Z. Fan, Engineering graphene aerogels with porous carbon of large surface area for flexible all-solid-state supercapacitors, Electrochim. Acta 165 (2015) 92–97, https://doi.org/10.1016/j.electacta.2015.02.008.

[16] Q. Zheng, B. Zhang, X. Lin, X. Shen, N. Yousefi, Z.-D. Huang, Z. Li, J.-K. Kim, Highly transparent and conducting ultralarge graphene oxide/single-walled carbon nanotube hybrid films produced by Langmuir–Blodgett assembly, J. Mater. Chem. 22 (2012) 25072–25082, https://doi.org/10.1039/C2JM34870E.

[17] P. Feng, S. Peng, P. Wu, C. Gao, W. Huang, Y. Deng, T. Xiao, C. Shuai, A nano-sandwich construct built with graphene nanosheets and carbon nanotubes enhances mechanical properties of hydroxyapatite–polyetheretherketone scaffolds, Int. J. Nanomedicine (2016) 3487–3500, https://doi.org/10.2147/IJN.S110920.

[18] H. Choi, H. Kim, S. Hwang, W. Choi, M. Jeon, Dye-sensitized solar cells using graphene-based carbon nano composite as counter electrode, Sol. Energy Mater. Sol. Cells 95 (2011) 323–325, https://doi.org/10.1016/j.solmat.2010.04.044.

[19] V. Sridhar, I. Lee, H.-H. Chun, H. Park, Microwave synthesis of nitrogen-doped carbon nanotubes anchored on graphene substrates, Carbon 87 (2015) 186–192, https://doi.org/10.1016/j.carbon.2015.01.063.

[20] X. Gan, R. Lv, J. Bai, Z. Zhang, J. Wei, Z.-H. Huang, H. Zhu, F. Kang, M. Terrones, Efficient photovoltaic conversion of graphene–carbon nanotube hybrid films grown from solid precursors, 2D Mater. 2 (2015) 034003, https://doi.org/10.1088/2053-1583/2/3/034003.

[21] R. Zeng, H. Deng, Y. Xiao, J. Huang, K. Yuan, Y. Chen, Cross-linked graphene/carbon nanotube networks with polydopamine "glue" for flexible supercapacitors, Compos. Commun. 10 (2018) 73–80, https://doi.org/10.1016/j.coco.2018.07.002.

[22] R. Shu, G. Zhang, J. Zhang, X. Wang, M. Wang, Y. Gan, J. Shi, J. He, Fabrication of reduced graphene oxide/multi-walled carbon nanotubes/zinc ferrite hybrid composites as high-performance microwave absorbers, J. Alloys Compd. 736 (2018) 1–11, https://doi.org/10.1016/j.jallcom.2017.11.084.

[23] A. Ashok, A. Kumar, J. Ponraj, S.A. Mansour, Synthesis and growth mechanism of bamboo like N-doped CNT/Graphene nanostructure incorporated with hybrid metal nanoparticles for overall water splitting, Carbon 170 (2020) 452–463, https://doi.org/10.1016/j.carbon.2020.08.047.

[24] T.T. Tung, M. Moussa, K.M. Tripathi, T. Kim, M.J. Nine, A.K. Nanjundan, D. Dubal, D. Losic, Coupling graphene microribbons with carbon nanofibers: new carbon hybrids for high-performing lithium and potassium-ion batteries, Sustainable Mater. Technol. 32 (2022) e00393, https://doi.org/10.1016/j.susmat.2022.e00393.

[25] S. Fang, L. Shen, H. Zheng, X. Zhang, Ge–graphene–carbon nanotube composite anode for high performance lithium-ion batteries, J. Mater. Chem. A 3 (2015) 1498–1503, https://doi.org/10.1039/C4TA04350B.

[26] J. Cui, S. Yao, J.-Q. Huang, L. Qin, W.G. Chong, Z. Sadighi, J. Huang, Z. Wang, J.-K. Kim, Sb-doped SnO_2/graphene-CNT aerogels for high performance Li-ion and Na-ion battery anodes, Energy Storage Mater. 9 (2017) 85–95, https://doi.org/10.1016/j.ensm.2017.06.006.

[27] G.D. Park, J.H. Kim, S.-K. Park, Y.C. Kang, $MoSe_2$ embedded CNT-reduced graphene oxide composite microsphere with superior sodium ion storage and electrocatalytic hydrogen evolution performances, ACS Appl. Mater. Interfaces 9 (2017) 10673–10683, https://doi.org/10.1021/acsami.7b00147.

[28] J. Luo, H.D. Jang, T. Sun, L. Xiao, Z. He, A.P. Katsoulidis, M.G. Kanatzidis, J. M. Gibson, J. Huang, Compression and aggregation-resistant particles of crumpled soft sheets, ACS Nano 5 (2011) 8943–8949, https://doi.org/10.1021/nn203115u.

[29] G.D. Park, J.S. Cho, Y.C. Kang, Novel cobalt oxide-nanobubble-decorated reduced graphene oxide sphere with superior electrochemical properties prepared by nanoscale Kirkendall diffusion process, Nano Energy 17 (2015) 17–26, https://doi.org/10.1016/j.nanoen.2015.07.026.

[30] S.H. Choi, Y.C. Kang, Crumpled graphene–molybdenum oxide composite powders: preparation and application in lithium-ion batteries, ChemSusChem 7 (2014) 523–528, https://doi.org/10.1002/cssc.201300838.

[31] S.Y. Jeong, S.-K. Park, Y.C. Kang, J.S. Cho, One-dimensional nanostructure comprising $MoSe_2$ nanosheets and carbon with uniformly defined nanovoids as an anode for high-performance sodium-ion batteries, Chem. Eng. J. 351 (2018) 559–568, https://doi.org/10.1016/j.cej.2018.06.130.

[32] M. Arjmand, K. Chizari, B. Krause, P. Pötschke, U. Sundararaj, Effect of synthesis catalyst on structure of nitrogen-doped carbon nanotubes and electrical conductivity and electromagnetic interference shielding of their polymeric nanocomposites, Carbon 98 (2016) 358–372, https://doi.org/10.1016/j.carbon.2015.11.024.

[33] J.H. Hong, G.D. Park, Y.C. Kang, Aerosol-assisted synthesis of bimetallic nanoparticle-loaded bamboo-like N-doped carbon nanotubes as an efficient bifunctional oxygen catalyst for Zn-air batteries, Int. J. Energy Res. 46 (2022) 5215–5225, https://doi.org/10.1002/er.7513.

[34] X. Ma, J. Chen, W. Zhao, Construction of series-wound architectures composed of metal–organic framework-derived hetero-(CoFe)Se_2 hollow nanocubes confined

into a flexible carbon skeleton as a durable sodium storage anode, Nanoscale 12 (2020) 22161–22172, https://doi.org/10.1039/D0NR05345G.
[35] J.Y. Lee, G.D. Park, J.H. Choi, Y.C. Kang, Structural combination of polar hollow microspheres and hierarchical N-doped carbon nanotubes for high-performance Li–S batteries, Nanoscale 12 (2020) 2142–2153, https://doi.org/10.1039/C9NR09807K.
[36] Z. Zhou, X. Gao, J. Yan, D. Song, Doping effects of B and N on hydrogen adsorption in single-walled carbon nanotubes through density functional calculations, Carbon 44 (2006) 939–947, https://doi.org/10.1016/j.carbon.2005.10.016.
[37] J. Zhang, E. Ha, D. Li, S. He, L. Wang, S. Kuang, J. Hu, Dual enzyme-like Co–$FeSe_2$ nanoflowers with GSH degradation capability for NIR II-enhanced catalytic tumor therapy, J. Mater. Chem. B 11 (2023) 4274–4286, https://doi.org/10.1039/D3TB00220A.
[38] S. Kim, S.J. Park, O. Park, H. Park, M. Heo, H.-S. Kim, S.-i. Kim, Phase formation and thermoelectric properties of $FeSe_2$–$CoSe_2$ system, Solid State Sci. (2023) 107236, https://doi.org/10.1016/j.solidstatesciences.2023.107236.
[39] X.-L. Wang, W.-Q. Han, J. Chen, J. Graetz, Single-crystal intermetallic M-Sn (M=Fe, Cu, Co, Ni) nanospheres as negative electrodes for lithium-ion batteries, ACS Appl. Mater. Interfaces 2 (2010) 1548–1551, https://doi.org/10.1021/am100218v.
[40] L. Yu, J. Liu, X. Xu, L. Zhang, R. Hu, J. Liu, L. Yang, M. Zhu, Metal-organic framework-derived NiSb alloy embedded in carbon hollow spheres as superior lithium-ion battery anodes, ACS Appl. Mater. Interfaces 9 (2017) 2516–2525, https://doi.org/10.1021/acsami.6b14233.
[41] J. Li, X. Xu, Z. Luo, C. Zhang, X. Yu, Y. Zuo, T. Zhang, P. Tang, J. Arbiol, J. Llorca, Compositionally tuned Ni_xSn alloys as anode materials for lithium-ion and sodium-ion batteries with a high pseudocapacitive contribution, Electrochim. Acta 304 (2019) 246–254, https://doi.org/10.1016/j.electacta.2019.02.098.
[42] G.D. Park, J.H. Hong, J.H. Choi, J.H. Lee, Y.S. Kim, Y.C. Kang, Synthesis process of $CoSeO_3$ microspheres for unordinary Li-ion storage performances and mechanism of their conversion reaction with Li ions, Small 15 (2019) 1901320, https://doi.org/10.1002/smll.201901320.
[43] M. Karthikayini, T. Thirupathi, G. Wang, V.K. Ramani, R. Raman, Highly active and durable non-precious metal catalyst for the oxygen reduction reaction in acidic medium, J. Electrochem. Soc. 163 (2016) F539, https://doi.org/10.1149/2.1001606jes.
[44] G.D. Park, Y.C. Kang, Amorphous cobalt selenite nanoparticles decorated on a graphitic carbon hollow shell for high-rate and ultralong cycle life lithium-ion batteries, ACS Sustain. Chem. Eng. 8 (2020) 17707–17717, https://doi.org/10.1021/acssuschemeng.0c05658.
[45] D. Liu, C. Wu, M. Yan, J. Wang, Correlating the microstructure, growth mechanism and magnetic properties of FeSiAl soft magnetic composites fabricated via HNO_3 oxidation, Acta Mater. 146 (2018) 294–303, https://doi.org/10.1016/j.actamat.2018.01.001.
[46] S.H. Yang, Y.J. Lee, H. Kang, S.-K. Park, Y.C. Kang, Carbon-coated three-dimensional MXene/iron selenide ball with core–shell structure for high-performance potassium-ion batteries, Nano-Micro Lett. 14 (2022) 1–17, https://doi.org/10.1007/s40820-021-00741-0.
[47] D. Kong, H. Wang, Z. Lu, Y. Cui, $CoSe_2$ nanoparticles grown on carbon fiber paper: an efficient and stable electrocatalyst for hydrogen evolution reaction, J. Am. Chem. Soc. 136 (2014) 4897–4900, https://doi.org/10.1021/ja501497n.
[48] S.H. Yang, S.K. Park, G.D. Park, J.H. Lee, Y.C. Kang, Conversion reaction mechanism of ultrafine bimetallic Co-Fe selenides embedded in hollow mesoporous carbon nanospheres and their excellent K-ion storage performance, Small 16 (2020) 2002345, https://doi.org/10.1002/smll.202002345.
[49] J.Y. Lee, N.Y. Kim, D.Y. Shin, H.-Y. Park, S.-S. Lee, S. Joon Kwon, D.-H. Lim, K. W. Bong, J.G. Son, J.Y. Kim, Nitrogen-doped graphene-wrapped iron nanofragments for high-performance oxygen reduction electrocatalysts, J. Nanopart. Res. 19 (2017) 98, https://doi.org/10.1007/s11051-017-3793-y.
[50] Y. Zhang, X. Yin, H. Jiang, J. Hao, Y. Wang, J. Yu, D. Li, Y. Liu, J. Li, Cobalt nanoparticles embedded in nitrogen-doped carbon nanotubes for efficient catalysis of oxygen reduction reaction, J. Iran. Chem. Soc. 16 (2019) 2575–2585, https://doi.org/10.1007/s13738-019-01722-2.
[51] F. Zheng, K. Chu, Y. Yang, Z. Li, L. Wei, Y. Xu, G. Yao, Q. Chen, Optimizing the interlayer spacing of heteroatom-doped carbon nanofibers toward ultrahigh potassium-storage performances, ACS Appl. Mater. Interfaces 14 (2022) 9212–9221, https://doi.org/10.1021/acsami.1c24275.
[52] Z. Ju, P. Li, G. Ma, Z. Xing, Q. Zhuang, Y. Qian, Few layer nitrogen-doped graphene with highly reversible potassium storage, Energy Storage Mater. 11 (2018) 38–46, https://doi.org/10.1016/j.ensm.2017.09.009.
[53] P. Xiong, X. Zhao, Y. Xu, Nitrogen-doped carbon nanotubes derived from metal–organic frameworks for potassium-ion battery anodes, ChemSusChem 11 (2018) 202–208, https://doi.org/10.1002/cssc.201701759.
[54] J. Zhao, H. Wu, L. Li, S. Lu, H. Mao, S. Ding, A $CoSe_2$-based 3D conductive network for high-performance potassium storage: enhancing charge transportation by encapsulation and restriction strategy, Mater. Chem. Front. 5 (2021) 5351–5360, https://doi.org/10.1039/D1QM00362C.
[55] Y. Liu, C. Yang, Y. Li, F. Zheng, Y. Li, Q. Deng, W. Zhong, G. Wang, T. Liu, $FeSe_2$/nitrogen-doped carbon as anode material for potassium-ion batteries, Chem. Eng. J. 393 (2020) 124590, https://doi.org/10.1016/j.cej.2020.124590.
[56] X. Ou, X. Liang, F. Zheng, P. Wu, Q. Pan, X. Xiong, C. Yang, M. Liu, In situ X-ray diffraction investigation of $CoSe_2$ anode for Na-ion storage: effect of cut-off voltage on cycling stability, Electrochim. Acta 258 (2017) 1387–1396, https://doi.org/10.1016/j.electacta.2017.11.198.
[57] Q. Peng, S. Zhang, H. Yang, B. Sheng, R. Xu, Q. Wang, Y. Yu, Boosting potassium storage performance of the Cu_2S anode via morphology engineering and electrolyte chemistry, ACS Nano 14 (2020) 6024–6033, https://doi.org/10.1021/acsnano.0c01681.
[58] Y. Xu, T. Ding, D. Sun, X. Ji, X. Zhou, Recent advances in electrolytes for potassium-ion batteries, Adv. Funct. Mater. 33 (2023) 2211290, https://doi.org/10.1002/adfm.202211290.
[59] T. Zhang, Y. Zhu, Y. Lv, Q. Yu, S. Yao, W. Zhu, Z. He, N-doped biomass carbon materials as superior catalyst to improve electrochemical performance of vanadium redox flow battery, Ionics 27 (2021) 4771–4781, https://doi.org/10.1007/s11581-021-04236-1.
[60] Z. Sun, X.L. Wu, J. Xu, D. Qu, B. Zhao, Z. Gu, W. Li, H. Liang, L. Gao, Y. Fan, Construction of bimetallic selenides encapsulated in nitrogen/sulfur co-doped hollow carbon nanospheres for high-performance sodium/potassium-ion half/full batteries, Small 16 (2020) 1907670, https://doi.org/10.1002/smll.201907670.
[61] C.A. Etogo, H. Huang, H. Hong, G. Liu, L. Zhang, Metal–organic-frameworks-engaged formation of $Co_{0.85}Se$@C nanoboxes embedded in carbon nanofibers film for enhanced potassium-ion storage, Energy Storage Mater. 24 (2020) 167–176, https://doi.org/10.1016/j.ensm.2019.08.022.
[62] H. Min, M. Li, H. Shu, X. Zhang, T. Hu, W. Wang, Y. Zhou, J. Jian, X. Wang, $FeSe_2$ nanoparticle embedded in 3D honeycomb-like N-doped carbon architectures coupled with electrolytes engineering boost superior potassium ion storage, Electrochim. Acta 366 (2021) 137381, https://doi.org/10.1016/j.electacta.2020.137381.
[63] H. Zhang, Y. Cheng, Q. Zhang, W. Ye, X. Yu, M.-S. Wang, Fast and durable potassium storage enabled by constructing stress-dispersed Co_3Se_4 nanocrystallites anchored on graphene sheets, ACS Nano 15 (2021) 10107–10118, https://doi.org/10.1021/acsnano.1c01918.
[64] J. Ge, L. Fan, J. Wang, Q. Zhang, Z. Liu, E. Zhang, Q. Liu, X. Yu, B. Lu, $MoSe_2$/N-doped carbon as anodes for potassium-ion batteries, Adv. Energy Mater. 8 (2018) 1801477, https://doi.org/10.1002/aenm.201801477.
[65] J.-S. Park, S.Y. Yang, J.-K. Lee, Y.C. Kang, A novel strategy for encapsulating metal sulfide nanoparticles inside hollow carbon nanosphere-aggregated microspheres for efficient potassium ion storage, J. Mater. Chem. A 10 (2022) 17790–17800, https://doi.org/10.1039/D2TA05678J.
[66] J.K. Kim, S.-K. Park, J.-S. Park, Y.C. Kang, Uniquely structured composite microspheres of metal sulfides and carbon with cubic nanorooms for highly efficient anode materials for sodium-ion batteries, J. Mater. Chem. A 7 (2019) 2636–2645, https://doi.org/10.1039/C8TA11481A.
[67] H.Y. Seo, J.H. Choi, Y.B. Kim, J.S. Cho, Y.C. Kang, G.D. Park, Tailoring the shell thickness of yolk–shell structured carbon microspheres: applications in metal selenide and carbon composite microspheres for enhanced sodium ion storage properties, J. Mater. Chem. A 11 (2023) 24738–24753, https://doi.org/10.1039/D3TA04705A.
[68] J. Yang, H. Gao, S. Men, Z. Shi, Z. Lin, X. Kang, S. Chen, $CoSe_2$ nanoparticles encapsulated by N-doped carbon framework intertwined with carbon nanotubes: high-performance dual-role anode materials for both Li-and Na-ion batteries, Adv. Sci. 5 (2018) 1800763, https://doi.org/10.1002/advs.201800763.
[69] S. Fan, G. Li, F. Cai, G. Yang, Synthesis of porous Ni-doped $CoSe_2$/C nanospheres towards high-rate and long-term sodium-ion half/full batteries, Chem. A Eur. J. 26 (2020) 8579–8587, https://doi.org/10.1002/chem.202000418.
[70] K. Zhang, M. Park, L. Zhou, G.H. Lee, W. Li, Y.M. Kang, J. Chen, Urchin-like $CoSe_2$ as a high-performance anode material for sodium-ion batteries, Adv. Funct. Mater. 26 (2016) 6728–6735, https://doi.org/10.1002/adfm.201602608.
[71] J. Chen, S. Li, K. Qian, P.S. Lee, NiMn layered double hydroxides derived multiphase Mn-doped Ni sulfides with reduced graphene oxide composites as anode materials with superior cycling stability for sodium ion batteries, Mater. Today Energy 9 (2018) 74–82, https://doi.org/10.1016/j.mtener.2018.02.008.
[72] K. Kisu, S. Aoyagi, H. Nagatomo, E. Iwama, M.T.H. Reid, W. Naoi, K. Naoi, Internal resistance mapping preparation to optimize electrode thickness and density using symmetric cell for high-performance lithium-ion batteries and capacitors, J. Power Sources 396 (2018) 207–212, https://doi.org/10.1016/j.jpowsour.2018.05.083.
[73] Y. Huang, S. Ding, S. Xu, Z.-F. Ma, J. Wang, X. Yuan, Highly effective solid electrolyte interface on SnO_2@C enabling stable potassium storage performance, Chem. Eng. J. 446 (2022) 137265, https://doi.org/10.1016/j.cej.2022.137265.
[74] B. Li, J. Zhao, Z. Zhang, C. Zhao, P. Sun, P. Bai, J. Yang, Z. Zhou, Y. Xu, Electrolyte-regulated solid-electrolyte interphase enables long cycle life performance in organic cathodes for potassium-ion batteries, Adv. Funct. Mater. 29 (2019) 1807137, https://doi.org/10.1002/adfm.201807137.
[75] F.J. Sonia, M.K. Jangid, M. Aslam, P. Johari, A. Mukhopadhyay, Enhanced and faster potassium storage in graphene with respect to graphite: a comparative study with lithium storage, ACS Nano 13 (2019) 2190–2204, https://doi.org/10.1021/acsnano.8b08867.
[76] D. Li, X. Ren, Q. Ai, Q. Sun, L. Zhu, Y. Liu, Z. Liang, R. Peng, P. Si, J. Lou, Facile fabrication of nitrogen-doped porous carbon as superior anode material for potassium-ion batteries, Adv. Energy Mater. 8 (2018) 1802386, https://doi.org/10.1002/aenm.201802386.
[77] Y. Jiang, J. Liu, Definitions of pseudocapacitive materials: a brief review, Energy Environ. Mater. 2 (2019) 30–37, https://doi.org/10.1002/eem2.12028.
[78] J. Wang, J. Polleux, J. Lim, B. Dunn, Pseudocapacitive contributions to electrochemical energy storage in TiO_2 (anatase) nanoparticles, J. Phys. Chem. C 111 (2007) 14925–14931, https://doi.org/10.1021/jp074464w.
[79] C. Zhang, Y. Xu, M. Zhou, L. Liang, H. Dong, M. Wu, Y. Yang, Y. Lei, Potassium Prussian blue nanoparticles: a low-cost cathode material for potassium-ion batteries, Adv. Funct. Mater. 27 (2017) 1604307, https://doi.org/10.1002/adfm.201604307.